

pubs.acs.org/cm Article

Covellite Nanodisks and Digenite Nanorings: Colloidal Synthesis, Phase Transitions, and Optical Properties

Mengqi Sun, Nicholas Kreis, Kexun Chen, Xiaoqi Fu, Song Guo,* and Hui Wang*



Cite This: Chem. Mater. 2021, 33, 8546-8558



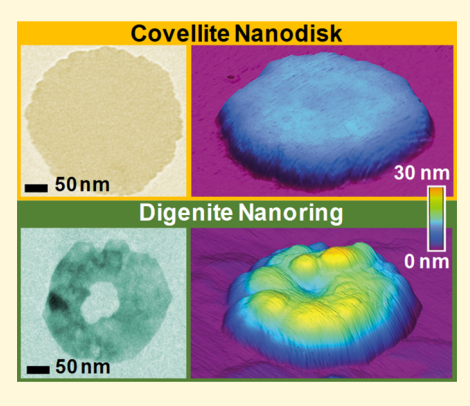
ACCESS

Metrics & More



Supporting Information

ABSTRACT: Copper sulfide nanoparticles represent a class of dual-functional materials whose optical properties are dominated by interband electronic transitions and intraband plasmon resonances, both of which can be systematically tuned by tailoring the geometric parameters and chemical compositions of the nanoparticles. Here, we report a temperature-programmed synthetic approach to monolithic covellite (CuS) nanodisks with thicknesses of around 11 nm and lateral diameters widely tunable in the range of ~100–300 nm. Our synthetic approach expands the aspect ratio-tuning range of covellite nanodisks typically achievable through previously developed colloidal syntheses, thereby enabling us to extend the plasmonic tunability of covellite nanodisks across near-infrared deep into mid-infrared. Covellite nanodisks with even larger lateral diameters beyond 300 nm, each of which is composed of stacked monolithic layers, can be synthesized either by increasing precursor concentrations or through seed-mediated nanodisk overgrowth. The superimposition of horizontally twisted covellite lattices in stacked monolithic layers gives rise to the



emergence of Moiré patterns on individual nanodisks in transmission electron microscopy images. Upon thermal treatment, monolithic covellite nanodisks dispersed in tetraethylene glycol transform into multicrystalline digenite (Cu_{1.8}S) nanorings through a postsynthesis phase-transitioning process, which not only further modifies plasmonic properties but also leads to energy shifts of the band gap and Fermi level of the nanoparticles. As revealed by the results of correlated atomic force microscopy and Kelvin probe force microscopy measurements, the local surface work functions of the covellite nanodisks and digenite nanorings in the size regime investigated in this work are essentially independent of the local surface topographic features and the way in which the quasi-two-dimensional nanostructures are stacked.

■ INTRODUCTION

Nanoparticles of noble metals, especially Au and Ag, represent so far the most intensively studied prototypical plasmonic materials widely utilized for applications ranging from optical imaging and spectroscopies to photocatalysis and biomedi-The past decade, however, has witnessed a continuously growing interest in searching for alternative plasmonic materials composed of earth-abundant non-noble metal elements, aiming at further enhancing plasmonic performance while mitigating cost issues for real-world applications. A variety of semiconductor materials, such as metal oxides, chalcogenides, phosphides, and nitrides, 33,34 become metal-like with emerging plasmonic features when cation/anion vacancies or ionized dopants are incorporated into their crystal lattices. In contrast to their metallic analogs whose plasmonic behaviors are dictated by the delocalized conduction electrons, nanoparticles of doped semiconductors support localized plasmon resonances arising from the collective oscillation of free holes in their valence bands. 11,35-37 Copper sulfide nanocrystals, which may versatilely adopt a variety of polymorphic crystalline phases accommodating a wide range of Cu/S stoichiometries,³³ emerged as a class of highly tunable, dual-functional materials

integrating excitonic properties of semiconductors with metal-like plasmonic behaviors. Covellite (CuS), the most Cudeficient, fully stoichiometric member in the copper sulfide family, exhibits intrinsic plasmonic characteristics due to its high free hole concentration ($\sim 10^{22}$ cm⁻³), whereas the most Cu-rich stoichiometric phase, chalcocite (Cu₂S), is plasmonically inactive due to the lack of free holes in its valence band. Chalcocite is thermodynamically unstable, spontaneously evolving into Cu-deficient Cu_{2-x}S phases (0 < x < 1) that are plasmonically active, such as djurleite (Cu_{1.96}S), digenite (Cu_{1.8}S), and anilite (Cu_{1.75}S), upon introduction of Cu vacancies into the crystal lattices. These nonstoichiometric Cu_{2-x}S materials are self-doped p-type semiconductors whose plasmon resonance frequencies can be fine-tuned by adjusting the free hole concentration in Cu_{2-x}S, which is tied to

Received: September 20, 2021 Revised: October 18, 2021 Published: October 28, 2021





the Cu/S stoichiometric ratios. ^{19,20,28,39} The variation of the Cu/S stoichiometries not only changes plasmonic properties but also shifts the Fermi level and alters conduction/valence band energies, ^{19,39} thereby remarkably modifying the excitonic properties of the materials as well.

In quasi-two-dimensional (Q2D) nanostructures such as nanodisks, nanosheets, and polygonal nanoplates, distinct optical properties may emerge upon selective excitations of the in-plane and out-of-plane excitonic and plasmonic modes. In a Q2D semiconductor nanoparticle, the valence-toconduction band gap for the out-of-plane excitations may differ significantly from that for the in-plane excitations due to quantum confinement effects. 43-45 The electronic band structures may be further modified, and new excitonic properties may emerge due to interlayer interactions when 2D nanostructured units are stacked together to form multilayered supra-nanostructures. 46-52 Besides the excitonic properties, the plasmonic properties of the Q2D nanostructures are also sensitively dependent on particle dimensions. For example, increasing the aspect ratios (lateral dimensions/ vertical thickness) of Au or Ag nanoplates leads to the frequency downshift of the in-plane plasmon modes all the way across the visible into near-infrared, while the out-of-plane plasmon resonances, which are remarkably less tunable, remain in the visible. 53-55 Switching from Au and Ag to covellite may further expand the plasmonic tunability of Q2D nanoparticles into mid-infrared because the free carrier concentration in covellite is about one order of magnitude lower than those in Au and Ag. 19,20,40 In addition, covellite has been considered as a better-performing plasmonic material in near-infrared and mid-infrared with significantly lower ohmic loss and, thus, less plasmon damping than Au and Ag. 42 Furthermore, unlike their noble metal counterparts whose free electron concentrations are essentially fixed, the free hole concentrations can be tuned when Q2D covellite nanocrystals undergo controlled phase transitions to form nonstoichiometric Cu_{2-x}S phases, ^{24,30} which further expands its plasmon tunability over even broader spectral ranges. Therefore, Q2D covellite nanoparticles and their nonstoichiometric Cu_{2-x}S derivatives constitute a unique materials system in which both the intraband plasmons and interband electronic transitions can be fine-engineered within a single nanoscale entity.

The most prevalent synthetic approach to colloidal Q2D copper sulfide nanocrystals involves the reactions of Cu(I) or Cu(II) salts with sulfur sources, most commonly elemental Sactivated by oleylamine and/or octadecene, in organic solvents at elevated temperatures through either one-pot heat-up or hot-injection processes. ^{24,28,40-42,56-61} An alternative synthetic route involves the thermal decomposition of single-source molecular precursors, such as Cu(II)-alkanethiolate, 62,63 Cu-(I)-thiobenzoate, 64 Cu(II)-O,O'-dialkyldithiophosphate, 65 and Cu(II)-diethyldithiocarbamate complexes. 66 The Q2D copper sulfide nanocrystals resulting from these colloidal syntheses typically exhibit monocrystalline disk-like or polygonal platelike morphologies with vertical thicknesses below 20 nm and lateral dimensions in the sub-100 nm regime. 24,28,30,40,49-61 The colloidal synthesis of Q2D copper sulfide nanocrystals with larger lateral sizes beyond 100 nm and higher aspect ratios, however, has been sparsely reported in the literature. 41,60 Here, we have developed a temperature-programmed heat-up method that enables us to systematically tune the lateral diameters of the monolithic covellite nanodisks ranging from ~100 to ~300 nm while keeping the nanodisk

thicknesses around 11 nm. Thicker covellite nanodisks composed of stacked monolithic layers with even larger lateral diameters beyond 300 nm can be synthesized by either increasing the precursor concentrations or using the monolithic nanodisks as the seeds to mediate the nanodisk overgrowth. The covellite nanodisks undergo phase transitions under thermal conditions to evolve into digenite nanorings. The broad tunability in the nanodisk aspect ratios leads to the expansion of the plasmon tuning range across the entire nearinfrared deep into mid-infrared, while the covellite-to-digenite phase transition further modifies the plasmonic features and shifts the Fermi level and the band gap energies of the nanoparticles. We have further investigated the relationship between the local surface topography and surface work functions on individual Q2D nanostructures, including monolithic covellite nanodisks, stacked covellite nanodisks, and digenite nanorings, through correlated atomic force microscopy (AFM) and Kelvin probe force microscopy (KPFM) measurements.

EXPERIMENTAL SECTION

Chemicals and Materials. Copper (II) nitrate trihydrate $(Cu(NO_3)_2 \cdot 3H_2O)$, ethylene glycol (EG), thiourea, polyvinylpyrrolidone (PVP, average molecular weight of 58,000), tetraethylene glycol (TEG), and ethanol (200 proof) were purchased from Alfa Aesar. All reagents were used as received without further purification.

Synthesis of Monolithic Covellite Nanodisks. Monolithic CuS nanodisks with an average thickness of ~11 nm and tunable average lateral diameters in the range of ~100-300 nm were synthesized through a temperature-programmed, one-pot heat-up process. In a typical procedure, 0.1 g of PVP was first dissolved in 8 mL of EG in a 50 mL round-bottom flask to form a clear solution, followed by the addition of 0.4 mL of 0.1 M Cu(NO₃)₂ and 1.6 mL of 0.1 M thiourea solutions (both Cu(NO₃)₂ and thiourea were dissolved in EG). A temperature-controlled heating mantle was used to quickly heat up the reactant mixtures from room temperature to 90 °C at a heating rate of ~6.5 °C min⁻¹. After the reaction temperature was maintained at 90 °C for 4 h, the reactant mixtures were heated up to 110 °C at a slow heating rate of 1 °C min⁻¹ and then maintained at 110 °C for 40 min to initiate the nucleation of CuS. The temperature was further raised to 130 °C at an even slower heating rate of 0.33 °C min⁻¹ to promote the anisotropic growth of CuS nanodisks. Finally, the temperature was maintained at 130 °C for another 50 min to allow the reactions to proceed to completion. The temporal evolution of the reaction temperature during the heat-up process was monitored in real time using a digital thermocouple (G1720 Precise Universal Thermometer, Priggen Special Electronic) directly immersed in the solvent. The entire reaction process was conducted in open air without any magnetic or mechanical stir. To obtain monolithic CuS nanodisks with various lateral diameters, 1 mL aliquots were withdrawn from the reactant mixtures at various times during the growth of the nanodisks, and the reaction was quenched by quickly cooling the samples in an ice bath. The kinetically trapped CuS nanodisks were collected through three cycles of centrifugation and redispersion in ethanol and finally stored in 1 mL of ethanol as colloidal suspensions. To investigate the effects of solution agitation, PVP, and heating profiles, control experiments were carried out under magnetic stirring, in a PVP-free environment, and following different temperature-programmed heating profiles, respectively.

Synthesis of Covellite Nanodisks Composed of Stacked Monolithic Layers. Larger CuS nanodisks composed of monolithic layers were synthesized by simply increasing the precursor concentrations without changing any other synthetic parameters. For example, CuS nanodisks with an average lateral diameter of \sim 380 nm and thickness of \sim 18 nm were synthesized by increasing the concentrations of Cu(NO₃)₂ and thiourea to 50 mM and 200 mM, respectively, in 10 mL of reactant mixtures while keeping the PVP

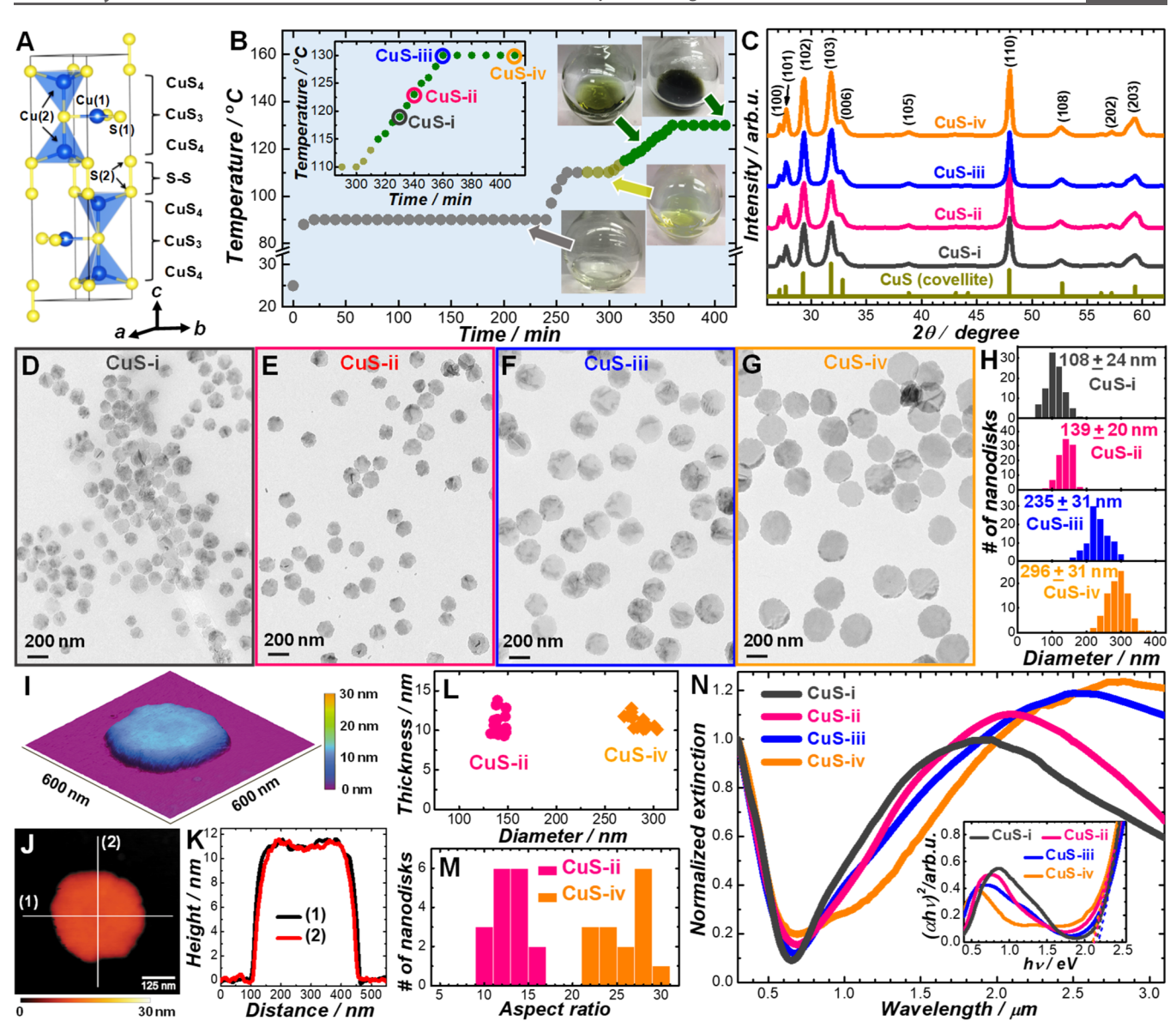


Figure 1. (A) Ball-and-stick model illustrating the unit cell structure of covellite (CuS). Reprinted with permission from ref 67. Copyright 2014 American Chemical Society. (B) Temporal evolution of the solution temperature during the temperature-programmed heat-up process for the synthesis of CuS nanodisks. Photographs of the colloidal nanoparticles formed at various stages are shown in the insets. The nanoparticle samples obtained at the reaction times of 330, 340, 360, and 410 min were labeled as CuS-i, CuS-ii, CuS-iii, and CuS-iv, respectively, as marked in the heating profile in the upper-left inset. (C) PXRD patterns of CuS-i, CuS-ii, CuS-iii, and CuS-iv. The PXRD patterns were offset for clarity. The standard pattern of covellite (JCPDS 6-464) were shown at the bottom as the reference. TEM images of (D) CuS-i, (E) CuS-ii, (F) CuS-iii, and (G) CuS-iv nanodisks. (H) The distributions of the lateral diameters of CuS-i, CuS-ii, CuS-iii, and CuS-iv nanodisks. The size distributions were obtained through analysis of 100 particles in TEM images of each sample. (I) 3D and (J) 2D representations of AFM topographic image and (K) topographic height profile along the lines (1) and (2) in (J) for an individual CuS-iv nanodisk. (L) Correlation between average diameter and thickness of individual CuS-ii and CuS-iv nanodisks revealed by AFM. (M) Distributions of the aspect ratios of CuS-ii and CuS-iv nanodisks revealed by AFM. (N) Optical extinction spectra of CuS-i, CuS-ii, CuS-iii, and CuS-iv nanodisks. The extinction spectra are shown after normalizing the extinction at 300 nm to 1. The Tauc plots are shown in the inset.

concentration and the temperature-programmed heating profile the same as those used for the synthesis of monolithic CuS nanodisks. Multilayered CuS nanodisks with an even larger average lateral diameter of ${\sim}600$ nm and average thickness of ${\sim}45$ nm were synthesized via a seed-mediated overgrowth process. Briefly, 200 μL of the as-synthesized colloidal monolithic CuS nanodisks (average thickness of 11 nm and lateral diameter of 296 nm) were redispersed in 8 mL of EG containing 0.1 g of PVP. Then, 0.2 mL of 0.1 M Cu(NO_3)_2 and 0.8 mL of 0.1 M thiourea were added. The reactant mixtures were thermally treated following a temperature-programmed heating profile that was the same as that for the synthesis of the monolithic CuS nanodisks. The resulting nanocrystals were collected

through centrifugation—redispersion cycles and finally dispersed in 1 mL of ethanol for storage.

Transformation of Covellite Nanodisks into Digenite Nanorings. The covellite-to-digenite phase transition occurred in TEG at 180 °C. In a typical procedure, 0.1 g of PVP was dissolved in 10 mL of TEG at room temperature. Then, the solution was heated up to 180 °C. Two hundred microliters of the as-synthesized monolithic nanodisks (average diameter of 296 nm and thickness of 11 nm) were quickly added, and the mixtures were maintained at 180 °C. The intermediate structures at various stages of phase transitions were kinetically trapped by taking out 1 mL aliquots at various reaction times and rapidly quenching the reactions in an ice bath. The

nanoparticles were washed with ethanol, collected through centrifugation, and finally stored in 1 mL of ethanol.

Characterizations. Transmission electron microscopy (TEM) images were taken using a Hitachi H-7800 transmission electron microscope operated at an accelerating voltage of 120 kV. Highresolution TEM (HRTEM) images were obtained using a JEOL JEM-2100 transmission electron microscope operated at an accelerating voltage of 200 kV. Scanning electron microscopy (SEM) images and energy dispersive spectroscopy (EDS) measurements were conducted using a Zeiss Ultraplus thermal field emission scanning electron microscope. Powder X-ray diffraction (PXRD) patterns were collected using a SAXSLab Ganesha at the South Carolina Collaborative (Cu $K_{\alpha} = 1.5405 \text{ Å}$). The optical extinction spectra were collected from nanoparticles dried on glass coverslips using a Cary 5000 UV/vis/NIR spectrophotometer. The Raman spectra were collected from nanoparticle samples supported on Si substrates in a back-scattering configuration under 785 nm laser excitations using a Bayspec Nomadic Raman microscope. The masses of Cu elements in various CuS nanodisk samples were quantified by mass spectrometry using a Finnigan ELEMENT XR double-focusing magnetic sector field inductively coupled plasma mass spectrometer (SF-ICP-MS) for the analysis of Cu (65 MR), with Rh (103 MR) serving as the internal standard. The nanoparticle samples were digested in 1 mL of nitric acid and 3 mL of hydrochloric acid in Teflon digestion vessels at 180 °C for 4 h. The digestates were brought to 100 mL with ultrapure H_2O (18.2 M Ω resistivity, Barnstead EasyPure II 7138) for the ICP-MS measurements

AFM topographies were constructed using semicontact mode on a NTEGRA Prima AFM (NT-MDT Spectrum Instruments). Contact potential difference (CPD) images were obtained using KPFM with dual-pass AM-SKM mode on the aforementioned instrument. For both AFM and KPFM, a MikroMasch HQ:NCS18/Pt tip (average resonance frequency: 55-65 kHz) was used. Substrates were cleaned by heating them in a 1:1:1 (v/v/v) solution of chlorobenzene/ acetonitrile/toluene for 15 min followed by 15 min of sonication. After cleaning, the solution was drained and replaced with filtered toluene (PTFE 1 μ m) for storing. Before spin-coating, substrates were removed from the filtered toluene solution as needed and treated with UV/Ozone for 3 min using an Ossila UV Ozone Cleaner. Samples for AFM and KPFM were prepared by spin-coating (2000 rpm, 1 min) 20 μ L of the respective CuS solution onto a cleaned substrate followed by a 10 s rinse with ethanol. Initial topography measurements were conducted using 5 × 7 mm silica wafers purchased from Ted Pella, Inc. Dual-pass (surface potential and topography) measurements were conducted on a grounded 1 × 1 cm ITO substrate (surface resistivity 70-100 Ω sq⁻¹) cut from a larger sheet purchased from Sigma-Aldrich. The constructed images were processed and analyzed using the open-source software Gwyddion.

■ RESULTS AND DISCUSSION

Covellite has a unique crystalline structure with built-in structural anisotropy, ^{38,67} which is distinct from the symmetric, face-centered cubic (fcc) structures that noble metals typically adopt. The growth of anisotropic nanostructures of fcc noble metals is typically guided by preformed seed particles, which are either multitwinned nanocrystals with intrinsic structural anisotropy^{68,69} or single-crystalline particles that undergo a critical symmetry-breaking process at the initiation stage of the seed-mediated nanocrystal growth. 70,71 Unlike their noble metal counterparts, the driving force for the growth of monolithic covellite nanodisks essentially originates from the intrinsic structural asymmetry of covellite itself. As illustrated in Figure 1A, covellite exhibits a layered structure perpendicular to the c axis of its unit cell. Each layer consists of alternating tetrahedral CuS₄ and trigonal planar CuS₃ units. The S atoms in the basal planes of the CuS4 units form covalent S-S bonds to hold two adjacent layers together. 38,67

Here, we developed a one-pot temperature-programmed heat-up method for the size-controlled synthesis of monolithic CuS nanodisks, in which Cu(I)-thiourea complexes, PVP, and EG served as the thermally decomposable precursor, surfacecapping ligands, and solvent, respectively. The reactions between Cu(NO₃), and thiourea in EG lead to the formation of Cu(I)-thiourea complexes with a general chemical formula of $[Cu_4(CS(NH_2)_2)_x](NO_3)_4$. It has been previously reported that the Cu(I)-thiourea complexes undergo thermal decomposition under solvothermal conditions at 150 °C to evolve into multicrystalline CuS microstructures composed of plate-shaped CuS units. 72,73 Success in synthesizing monolithic CuS nanodisks with high aspect ratios, however, requires the creation of a reaction environment that selectively promotes the in-plane growth of the nanocrystals while the thickening of the nanodisks, the formation of twinning sites, and the secondary nucleation on the growing nanodisk surfaces are all effectively suppressed. We found that through a deliberately designed and temperature-programmed heat-up process, the thermal decomposition of the Cu(I)-thiourea precursors, nucleation of CuS, and anisotropic in-plane growth of CuS nanodisks could all be kinetically maneuvered, enabling us to tune the lateral diameters of monolithic CuS nanodisks in the range of ~100-300 nm while keeping the nanodisk thicknesses around 11 nm. Figure 1B shows the temperatureprogrammed heating profile we adopted when developing a standard protocol for the synthesis of monolithic CuS nanodisks. The reactant mixtures were first maintained at 90 $^{\circ}$ C for 4 h to let $Cu(NO_3)_2$ fully react with thiourea until equilibrium was reached. The Cu(I)-thiourea complexes were colorless when dissolved in EG, consistent with previously reported observations. ^{72,73} The reaction temperature was then elevated to 110 °C at a heating rate of 1 °C min⁻¹ and maintained at 110 °C for another 40 min until the solution turned chartreuse in color, indicative of the formation of CuS nuclei. The CuS nanocrystals produced at the nucleation stage (kinetically trapped at the reaction time of 300 min during the temperature-programmed heat-up process) had a broad distribution of particle sizes and morphologies, and some of them had already started to develop embryotic disk-like shapes (Figure S1 in the Supporting Information). The reaction temperature was further raised to 130 °C at a slow heating rate of 0.33 °C min⁻¹ and maintained at 130 °C to promote the inplane growth of monolithic CuS nanodisks. During the growth of nanodisks, the color of the colloidal suspensions became increasingly deeper, gradually evolving from chartreuse to olive green (inset photographs in Figure 1B). The intermediate structures at various stages of the nanocrystal growth could be kinetically trapped by quenching the reaction in an ice bath and then isolated from the reactant mixtures through centrifugation and redispersion in ethanol. As illustrated in the upper left inset of Figure 1B, we captured the nanodisks at reaction times of 330, 340, 360, and 410 min during the temperature-programmed heat-up process, which were labeled as CuS-i, CuS-ii, CuS-iii, and CuS-iv, respectively. The PXRD patterns of the nanodisk samples were in excellent agreement with the standard pattern of hexagonal-phase covellite (JCPDS 6-464) without any detectable lattice distortion or other copper sulfide phases (Figure 1C). In comparison to the CuS nanocrystals produced at the nucleation stage, these CuS nanodisks exhibited more uniform disk-like shapes (Figures 1D-G) with much narrower size distributions (Figure 1H) primarily due to the Ostwald ripening of the nanocrystals

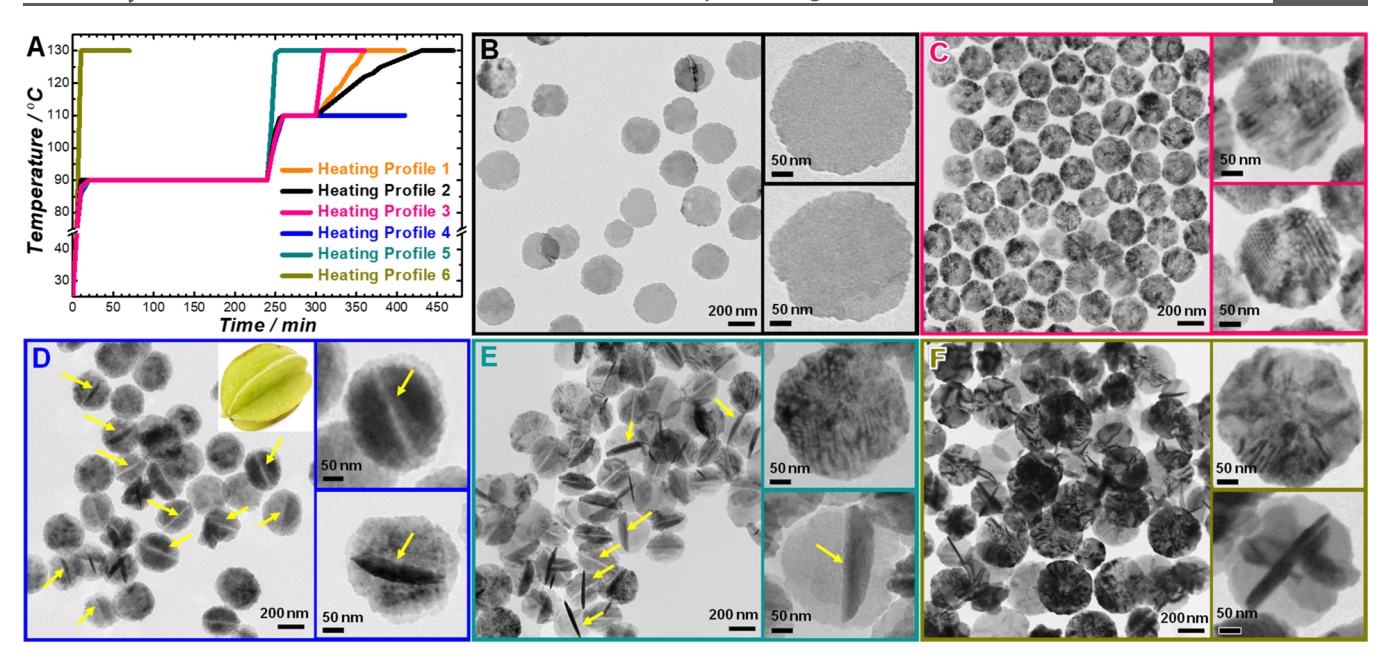


Figure 2. (A) Temporal evolutions of solution temperatures for the programmed heating profiles 1, 2, 3, 4, 5, and 6. TEM images of the nanoparticles synthesized through heating profiles (B) 2, (C) 3, (D) 4, (E) 5, and (F) 6. The left panels show the lower-magnification TEM images of multiple nanoparticles, and the right panels show the higher-magnification TEM images of individual nanoparticles. The stacking sites for multiple nanoplates with different orientations are labeled with yellow arrows. A photograph of a starfruit is also shown as an inset in (D).

during the nanodisk growth. The lateral diameters kept increasing while the disk shape was well preserved during the nanocrystal growth until the precursors were fully consumed after the reaction temperature was maintained at 130 °C for approximately 50 min (Figure S2 in the Supporting Information). Further increase in reaction time did not lead to any increase in the lateral diameters of the nanodisks (Figure S3 in the Supporting Information), suggesting the termination of nanodisk growth. Because of their relatively large aspect ratios, almost all CuS nanodisks lay down on the TEM grids, typically exhibiting a circular 2D profile in the TEM images (Figures 1D-G). The disk shape of the nanoparticles was further verified by TEM and SEM when the sample substrates were tilted with respect to the normal projection (Figures S4 and S5 in the Supporting Information). We used EDS to quantify Cu/S stoichiometric ratios of the covellite nanodisks according to the relative intensities of the Cu L and S K lines. The Cu/S atomic ratios were very close to 1:1 (Figure S6 in the Supporting Information), fully consistent with the expected value for covellite. Correlated SEM imaging/ EDS elemental mapping results revealed that the Cu and S elements were well mixed in each nanodisk rather than forming phase-segregated elemental domains (Figure S7 in the Supporting Information). In the HRTEM image (Figure S8 in the Supporting Information), the (110) lattice fringes of covellite were clearly resolved on a nanodisk projected along the [001] zone axis, and the fast Fourier transform (FFT) pattern of the HRTEM image (insets of Figure S8 in the Supporting Information) reflected the monocrystalline nature of the nanodisk.

Although the lateral diameter of each nanodisk could be accurately determined through TEM imaging, we were unable to directly measure the nanodisk thickness based on the TEM images due to the absence of "standing-up" nanodisks that are oriented perpendicularly to the TEM grids. Therefore, we used AFM to measure the surface topography and the thicknesses of

individual CuS nanodisks. Figures 1I-K show the AFM images and the topographic height profiles of an individual CuS-iv nanodisk that was ~11 nm thick, which exhibited a typical disk shape with a circular cross section and a relatively smooth surface. We collected the AFM images of multiple CuS-ii and CuS-iv nanodisks, and the average diameters and thicknesses of individual nanodisks were plotted in Figure 1L. The nanodisk diameters measured by AFM were in good agreement with those determined by TEM. Although the CuS-iv nanodisks were about twice as large as the CuS-ii nanodisks in terms of lateral diameters, the nanodisk thicknesses always remained around 11 nm, corresponding to the thickness of six to seven unit cells (lattice constant of covellite is 1.634 nm along the c axis). The AFM results revealed that under the current synthetic conditions, the nanodisks grew predominantly along the lateral in-plane direction, while growth along the c axis of the unit cell was effectively inhibited. Therefore, the growth of nanodisks led to an increase of their aspect ratios (Figure 1M), while the changes in their thicknesses remained minimal.

As shown in Figure 1N, the spectral features of various CuS nanodisk samples in the optical extinction spectra were dominated by a broad peak in near-infrared or mid-infrared associated with the optical excitations of the in-plane plasmon resonance modes. The broad bandwidths of the in-plane plasmon peaks were tied to the Q2D disk-like shape of the nanoparticles and the large imaginary part of the dielectric function of CuS in near- and mid-infrared. 42 As the aspect ratio of the nanodisks increased, the in-plane plasmon resonance progressively shifted toward longer wavelengths, which consolidated the aspect ratio dependency of the near-infrared plasmonic features previously observed on smaller CuS nanodisks. 42,74 Our synthetic approach offered the capability to tune the average aspect ratios of monolithic CuS nanodisks over a broader range up to \sim 27, enabling us to further extend the plasmonic tunability of CuS nanodisks across the entire near-infrared into mid-infrared. Because the free charge carrier

concentration in CuS is approximately one order of magnitude lower than those in noble metals, 19 the in-plane plasmons of CuS nanodisks are resonant at significantly longer wavelengths than those of their Au and Ag counterparts with comparable aspect ratios. In addition to the spectral features associated with the plasmon resonances, strong light absorption was also observed in visible light, which was a spectral feature of the valence-to-conduction interband transitions. The spectral features associated with the excitonic excitations, however, appeared independent of the aspect ratios of the CuS nanodisks. According to the Tauc plots (inset of Figure 1N), the direct band gap values of various CuS nanodisk samples were all in the range of 2.1-2.2 eV, consistent with the previously reported values of CuS materials. 19,75-77 We did not observe any band gap widening due to quantum confinement effect because both the lateral sizes and the thicknesses of the CuS nanodisks were larger than the Bohr radius of CuS. 19

Both the surface-capping ligand (PVP) and agitation of the reactant solution were found to be crucial factors influencing the morphological evolution of the CuS nanostructures. When the reaction occurred in the absence of PVP under otherwise identical conditions, irregularly shaped CuS nanostructures were formed instead of monolithic CuS nanodisks (Figure S9 in the Supporting Information), which indicated that PVP could selectively passivate the (100) facets of CuS and suppress crystal twinning and branching, thereby effectively promoting the lateral 2D growth of monolithic CuS nanodisks. Under our experimental conditions, monolithic CuS nanodisks were synthesized only when no agitation was applied to the reactant mixtures. When the reactions took place under magnetic stirring, the resulting CuS particles started to evolve into a branched morphology composed of CuS nanoplates (Figure S10 in the Supporting Information), which was most likely a consequence of twinning-induced, branched crystal growth triggered by solution agitation. The synergistic actions of surface capping by PVP and crystal twinning caused by agitation were best manifested by a control experiment carried out in the presence of a high concentration of PVP (six times of the PVP concentration in the standard synthetic protocol) with high-speed magnetic stirring (300 rpm), which led to the formation of flower-like, highly branched nanostructures consisting of thin CuS nanosheets (Figure S11 in the Supporting Information).

The temperature programming of the heating profiles played a crucial role in guiding the growth of monolithic CuS nanodisks. Figure 2A shows the temporal evolutions of reaction temperatures associated with six different heating profiles. The heating profile involved in the standard synthetic protocol (shown in Figure 1B) was labeled as heating profile 1. After the CuS nuclei were produced at 110 °C, the reaction temperature was slowly raised from 110 to 130 °C at a heating rate of 0.33 °C min⁻¹, which facilitated the 2D in-plane growth of monolithic CuS nanodisks. When further decreasing the heating rate to ~0.165 °C min⁻¹ (heating profile 2), the resulting CuS nanodisks appeared very similar to those synthesized through heating profile 1 in terms of both nanodisk morphology and lateral dimensions (Figure 2B). In contrast, a rapid elevation of temperature from 110 to 130 °C at a heating rate of ~2 °C min⁻¹ (heating profile 3) led to significant decrease in the average lateral diameter of the resulting CuS nanodisks (Figure 2C and Figure S12 in the Supporting Information). Interestingly, groups of parallel strips and/or 2D superlattice patterns were clearly observed on every

single nanodisk in the TEM images (Figure 2C), which were the Moiré patterns signifying the superimposition of two oblique CuS lattices sharing the common base vector along the c axis. 56,72 The fringe spacing and detailed patterns of the Moiré patterns varied significantly from site to site within the same nanodisks, suggesting different twist angles between two stacked layers in different regions. The uneven distributions of Moiré patterns on individual nanodisks further suggested a rugged surface topography of the nanodisks, which was confirmed by the AFM results (Figure S13 in the Supporting Information). These CuS nanodisks with Moiré patterns were about twice as thick as their monolithic counterparts synthesized through heating profile 1 (Figure 1I-K and Figure S13 in the Supporting Information) due to the stacking of two monolithic layers. Despite the difference in their lateral diameters and thicknesses, the CuS nanodisks synthesized through heating profiles 1 and 3 had similar volumes per particle when all the precursors were fully consumed. Our observations suggested that fast temperature elevation triggered the secondary nucleation on the growing nanodisks, which eventually led to the Moiré stacking of monolithic layers, whereas slow heat-up processes favored the 2D growth of monolithic nanodisks and suppressed the secondary nucleation.

If the reaction temperature was maintained at 110 °C after CuS nucleation (heating profile 4), the nuclei could still grow into larger nanocrystals at a slower growth rate than at 130 °C. In this case, each of the resulting nanoparticles were multicrystalline in nature with multiple nanoplates orientated differently to form branched structures that resembled starfruits (Figure 2D). The stacking sites where multiple nanoplates merged could be clearly visualized in the TEM images as labeled with yellow arrows in Figure 2D. The primary driving force for the formation of such branched nanostructures was most likely associated with the crystal twinning that occurred during the slow crystal growth at 110 °C. Following the standard heating profile 1, the kinetics of nucleation and nanocrystal growth were controlled separately, which favored the growth of monolithic nanodisks. However, if the reaction temperature was quickly increased from 90 to 130 °C at a heating rate of 4 °C min⁻¹ after incubating the reactant at 90 °C for 4 h (heating profile 5), both the nucleation and growth occurred rapidly and became kinetically entangled. As a result, the CuS nanoparticles evolved into two subpopulations: nanodisks with Moiré fringes and multibranched, starfruit-like nanocrystals (Figure 2E), indicating that both crystal twinning and secondary nucleation occurred during this fast heat-up process. In another control experiment, we directly heated up the reactant mixtures from room temperature to 130 °C at a heating rate of ~11 °C min⁻¹, during which both nucleation and nanocrystal growth occurred before the Cu(NO₃)₂ and thiourea were fully reacted to reach equilibrium. In this case, the resulting CuS nanoparticles exhibited a broad size distribution, and the particle shapes became nonuniform (Figure 2F) primarily due to lack of kinetic control over the precursor decomposition, nucleation, and crystal growth. The products were made up of smaller monolithic nanodisks, larger nanodisks with Moiré fringes, and multibranched nanoparticles analogous to the morphologies of the CuS samples previously synthesized through decomposition of Cu(I)-thiourea complexes under solvothermal conditions. 72,73

CuS nanodisks with even larger lateral diameters beyond 300 nm could be synthesized through the standard temper-

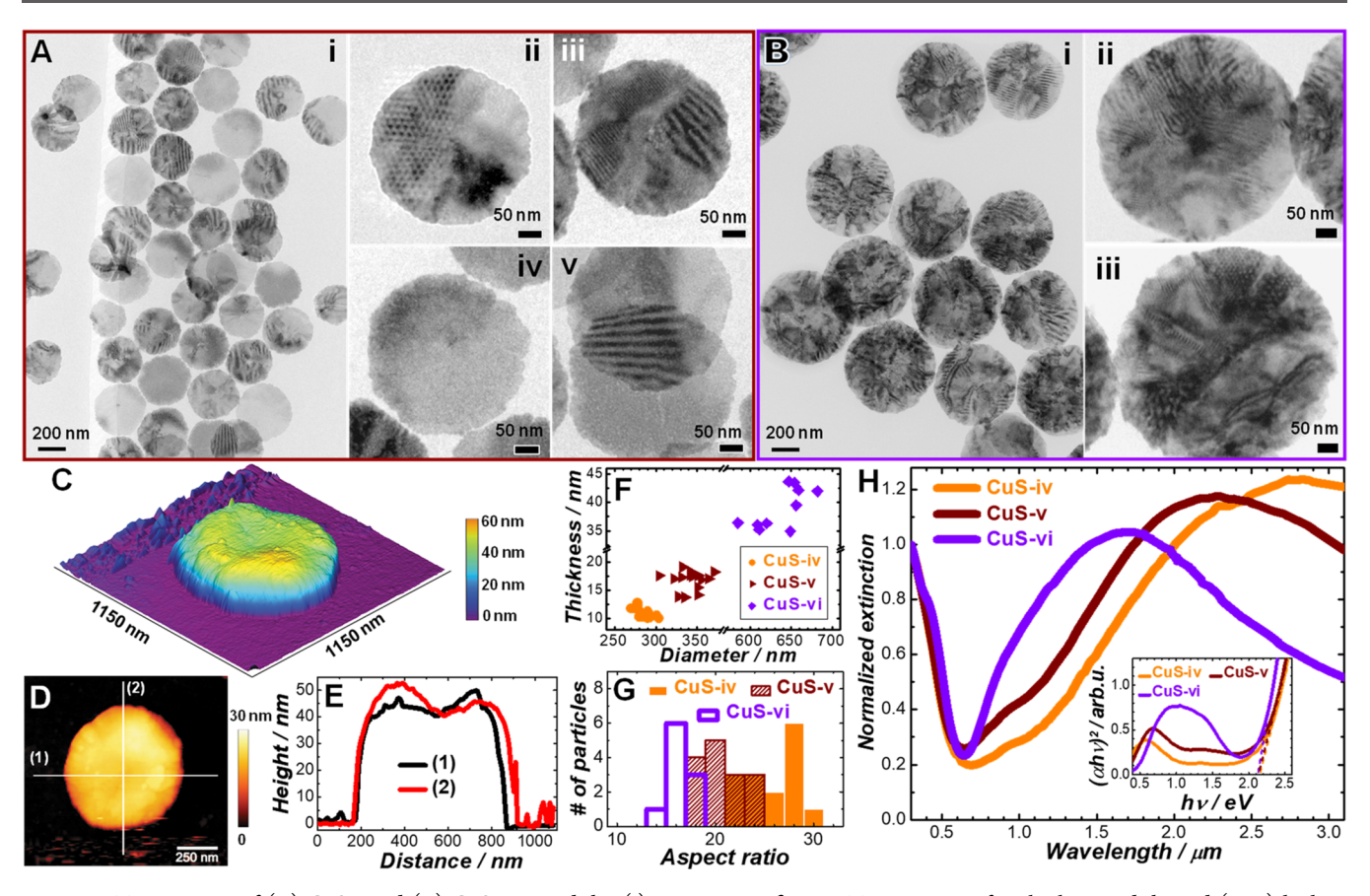


Figure 3. TEM images of (A) CuS-v and (B) CuS-vi nanodisks. (i) Lower-magnification TEM images of multiple nanodisks and (ii—v) higher-magnification TEM images highlighting individual nanodisks or partially stacked nanodisks. (C) 3D and (D) 2D representations of AFM topographic image and (E) topographic height profiles along lines (1) and (2) in (D) for an individual CuS-vi nanodisk. (F) Correlation between average diameter and thickness of individual CuS-iv, CuS-v, and CuS-vi nanodisks revealed by AFM. (G) Distributions of the aspect ratios of CuS-iv, CuS-v, and CuS-vi nanodisks revealed by AFM. (H) Optical extinction spectra of CuS-iv, CuS-v, and CuS-vi nanodisks. The extinction spectra are shown after normalizing the extinction at 300 nm to 1. The Tauc plots are shown in the inset.

ature-programmed heat-up process (heating profile 1) with higher concentrations of the precursors. When the $Cu(NO_3)_2$ concentration was varied from 1.6 mM for the standard protocol to 2.0 mM with the Cu/thiourea molar ratio still kept at 1:4, the average lateral diameters of the resulting CuS nanodisks, which were labeled as CuS-v, increased to 381 nm (Figure 3A). In the TEM images of the CuS-v sample, about 65% of the nanodisks exhibited Moiré patterns (Figure 3Aiiii), while the other ~35% of the nanodisks did not (Figure 3Ai,iv). The detailed features of the Moiré patterns varied from particle to particle, displaying either well-defined 2D superlattice patterns (Figure 3Aii) or parallel strips with varying fringe spacing (Figure 3Aiii). Moiré fringes were also observed where two nanodisks were partially stacked (Figure 3Av). The emergence of Moiré patterns on the CuS-v nanodisks could be interpreted as the consequence of the Moiré stacking of two CuS monolithic layers, suggesting that excessive precursors might be decomposed to form secondary nuclei on the surfaces of some growing nanodisks. About 1% of nanodisks in the CuS-v sample showed a unique structure with a seminanodisk sitting on top of a fully developed nanodisk (Figure S14 in the Supporting Information), which was an immature, intermediate structure kinetically trapped during the growth of CuS-v

Even larger CuS nanodisks were synthesized using the monolithic CuS-iv nanodisks as seeds to mediate the

overgrowth of the nanodisks through the temperatureprogrammed heat-up process (heating profile 1). As shown in Figure 3B, the overgrown nanodisks, which were labeled as CuS-vi, had an average lateral diameter as large as ~600 nm, and Moiré patterns were clearly observed on every single overgrown nanodisk (Figure 3B). The Moiré stacking of monolithic layers in the overgrown nanodisks was a direct consequence of secondary nucleation on the monolithic nanodisk seeds. AFM images clearly revealed that the overgrown nanodisks had rugged surfaces and were significantly thicker than the monolithic seeds (Figures 3C-E). The lateral diameters of CuS-iv, CuS-v, and CuS-vi nanodisks determined by the TEM were compared in Figure S15 in the Supporting Information. PXRD results further confirmed that both CuS-v and CuS-vi nanodisks were in the hexagonal covellite phase (Figure S16 in the Supporting Information). The characteristic Raman bands of the S-S stretching mode⁷⁴ were centered at 472 cm⁻¹ for both the monolithic CuS-iv and Cu-vi nanodisks with Moiré patterns (Figure S17 in Supporting Information), indicating that the Moiré stacking of monolithic layers did not cause any distortion to the S-S bonds in the covellite lattices. Therefore, as inferred by the Raman results, the primary interlayer forces responsible for the Moiré stacking of monolithic CuS layers in CuS-vi nanodisks were most likely the van der Waals interactions rather than the covalent S-S bonds. According to the results of AFM

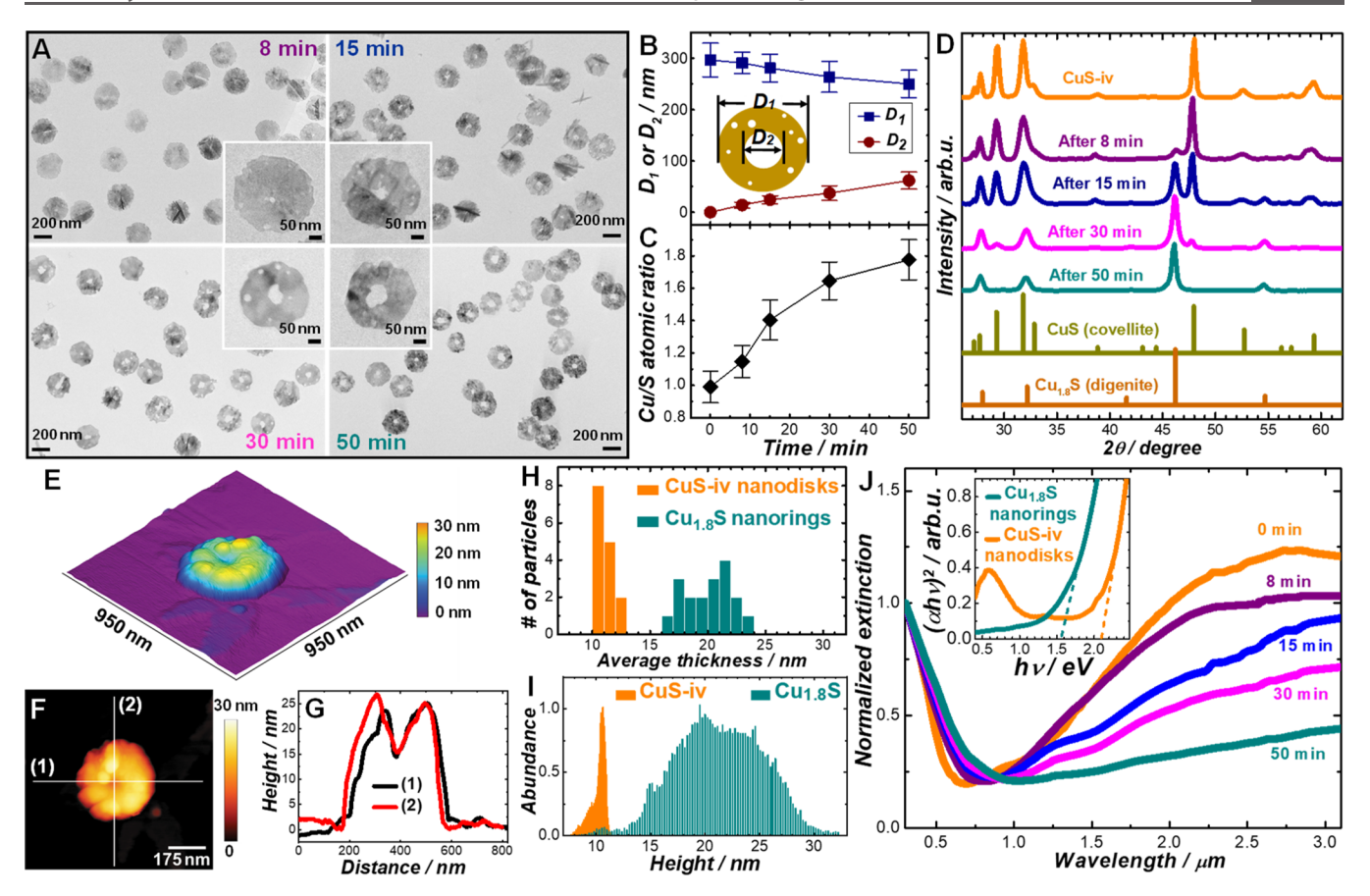


Figure 4. (A) TEM images of the nanorings formed at reaction times of 8, 15, 30, and 50 min during the covellite-to-digenite phase transitions. TEM images of individual nanoparticles are shown in the insets. The starting nanodisk sample for the phase transition is CuS-iv. (B) Temporal evolutions of the outer (D_1) and inner diameters (D_2) of the nanorings during the covellite-to-digenite phase transitions. (C) Temporal evolution of Cu/S atomic ratios during the covellite-to-digenite phase transitions. (D) PXRD patterns of the nanorings formed at reaction times of 8, 15, 30, and 50 min. Standard PXRD patterns of CuS (covellite, JCPDS 6-464) and Cu_{1.8}S (digenite, JCPDS 04-0784) are shown at the bottom for comparison. (E) 3D and (F) 2D representations of AFM topographic image and (G) topographic height profiles along the lines (1) and (2) in (F) for an individual Cu_{1.8}S nanoring (sample obtained after 50 min). (H) Distributions of the average thicknesses of CuS-iv nanodisks and Cu_{1.8}S nanorings revealed by AFM at the single-particle level. (I) Distributions of the thicknesses of CuS-iv nanodisks and Cu_{1.8}S nanorings revealed by AFM at the single-pixel level. (J) Optical extinction spectra of the nanorings formed at reaction times of 8, 15, 30, and 50 min during the covellite-to-digenite phase transitions. The extinction spectra are shown after normalizing the extinction at 300 nm to 1. The Tauc plots of CuS-iv nanodisks and Cu_{1.8}S nanorings are shown in the inset.

topographic measurements performed on multiple nanodisks in each sample, both lateral diameters and vertical thicknesses of the nanodisks increased in the order of CuS-iv < CuS-v < CuS-vi (Figure 3F). However, the aspect ratios of the nanodisks decreased in the order CuS-iv > CuS-v > CuS-vi (Figure 3G). As shown in Figure 3H, the resonance wavelengths of the in-plane plasmons supported by the nanodisks progressively blue-shifted as the aspect ratios decreased, whereas the band gap values appeared independent of the aspect ratios and the Moiré stacking of monolithic CuS layers.

Besides the size control of the CuS nanodisks, the optical properties could also be tuned by varying the Cu/S stoichiometric ratios through postsynthesis phase transitions. Manna and coworkers²⁴ observed that covellite nanodisks, upon exposure to a Cu(I) complex, [Cu(CH₃CN)₄]PF₆, evolved into nonstoichiometric Cu_{2-x}S phases as a consequence of intercalation of Cu(I) ions into the covellite lattices. Alternatively, as demonstrated by Swihart and coworkers,³⁰ the interlayer disulfur bonds in covellite nanodisks could be reduced by a mild reducing agent, 1-dodecanethiol (DDT), which led to the transformation of the covellite lattices into the

chalcocite phase. In both cases, the nanodisk morphology was well preserved during the phase transitions, although the lateral sizes and thicknesses of the nanodisks both changed within a certain range. 24,30 Here, we observed that colloidal monolithic covellite nanodisks evolved into digenite nanorings through phase transitions when dispersed in TEG at 180 °C, a unique structure-transforming process that has never been observed on copper sulfide nanocrystals before. Under our experimental condition, neither Cu(I) species nor additional reducing agents were needed to trigger the covellite-to-digenite phase transition because TEG served as a solvent with a built-in temperature-dependent reducing capability. 79,80 As shown in Figure 4A, the structural transformation was initiated upon the formation of a cavity in the center of each CuS nanodisk. As the phase transition proceeded, the central cavities gradually expanded in size accompanied by the emergence of an increasing number of smaller cavities in the nanorings. The smaller cavities became larger over time until they coalesced into larger cavities, while the central cavities kept expanding. Upon completion of the phase transition, the cavities in the intermediate structures merged into one central hole in each fully developed digenite nanoring. Therefore, the structural

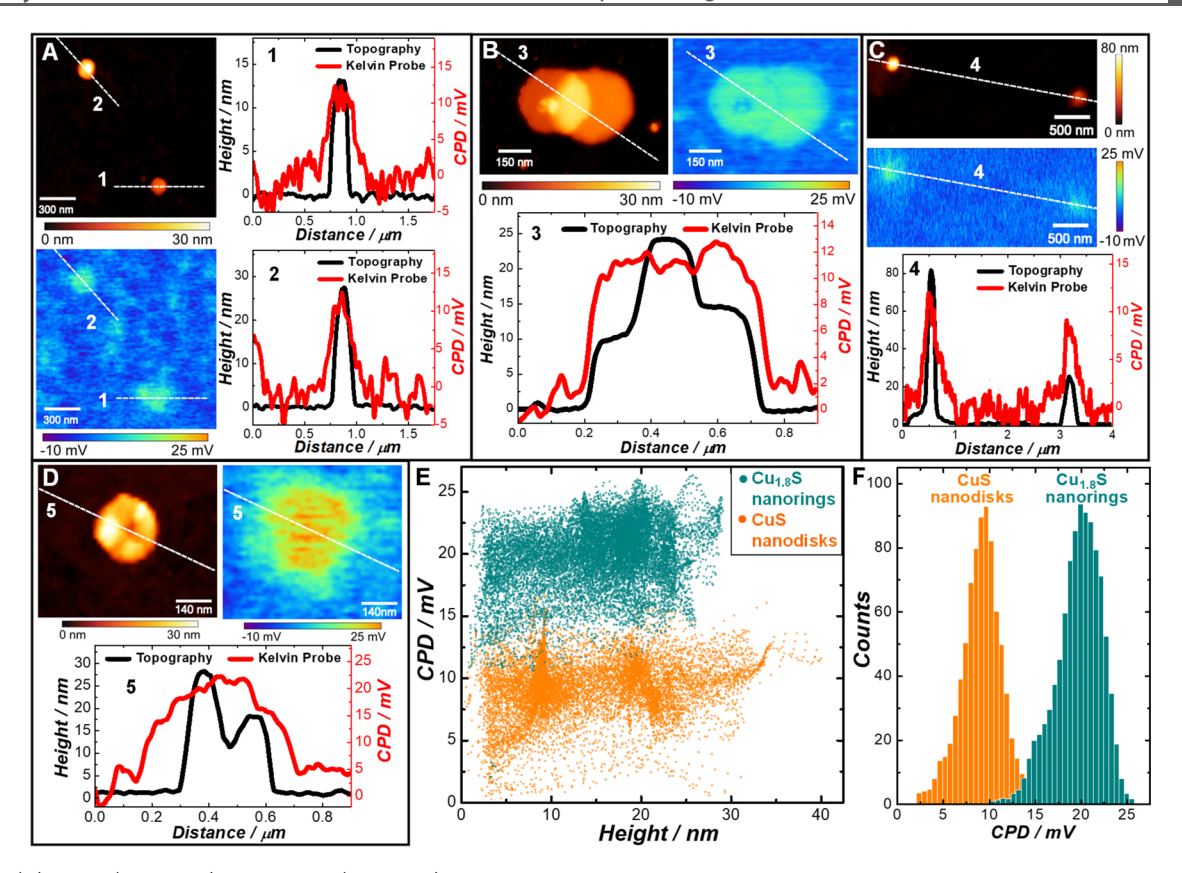


Figure 5. (A) AFM (upper left) and KPFM (lower left) images of CuS-ii nanodisks and topographic and CPD profiles along the lines 1 (upper right) and 2 (lower right). (B) AFM (upper left) and KPFM (upper right) images of two partially stacked CuS-iv nanodisks and topographic and CPD profiles along line 3 (bottom). (C) AFM image (top), KPFM image (middle), and topographic and CPD profiles along the line 4 (bottom) of CuS nanodisks synthesized through programmed heating profile 3. (D) AFM (upper left) and KPFM images (upper right) of an individual Cu_{1.8}S nanoring and topographic and CPD profiles along line 5 (bottom). (E) Correlation between CPD values and the sample heights (thicknesses) of CuS nanodisks and Cu_{1.8}S nanorings at the single-pixel level. (F) Histograms showing the distribution of CPD values of CuS nanodisks and Cu_{1.8}S nanorings.

evolution of the covellite nanodisks during the phase transition was intimately tied to the Ostwald ripening of the cavities. Under our experimental conditions, the covellite-to-digenite phase transition went to completion after ~50 min. Further increasing the reaction time to 120 min did not lead to any significant morphological or dimensional changes of the digenite nanorings (Figure S18 in the Supporting Information). During the nanodisk-to-nanoring transformations, the outer diameters of the nanorings (D_1) kept decreasing, while the diameters of the central cavities (D_2) increased continuously (Figure 4B and Figure S19 in the Supporting Information). The Cu/S stoichiometric ratios (quantified by EDS) kept increasing during the phase transitions, evolving from 0.99 \pm 0.10 for the starting covellite nanodisks (CuS-iv) to 1.78 ± 0.12 for the fully converted digenite nanorings (Figure 4C and Figure S20 in the Supporting Information). Covellite and digenite were the only two crystalline phases identified by PXRD during the phase transitions (Figure 4D). It was possible that other crystalline phases, such as yarrowite (Cu_{1.12}S) and anilite (Cu_{1.75}S), served as the intermediate structures during the covellite-to-digenite transitions. However, it was highly likely that these intermediate phases were shortlived and were, thus, not captured by ex situ PXRD measurements. In the Raman spectrum of Cu_{1.8}S nanorings, the characteristic peak of the S-S stretching mode completely disappeared (Figure S21 in the Supporting Information), indicating that the interlayer S-S bonds were cleaved when the

hexagonal covellite lattices were rearranged into cubic-phase digenite lattices. The substantial structural rearrangements of the lattices led to the conversion of monolithic nanodisks into multicrystalline nanorings, as revealed by the HRTEM image and its FFT pattern of an individual $\text{Cu}_{1.8}\text{S}$ nanoring (Figure S22 in the Supporting Information).

AFM images (Figures 4E-G) showed that the nanodisk-tonanoring transformation led to a significant increase in not only the thickness but also the surface roughness of the nanoparticles. On average, the Cu_{1.8}S nanorings derived from the CuS-iv nanodisks were twice as thick as their parental nanodisks (Figure 4H). The dip in the center of each Cu_{1.8}S nanoring was coincident with the location of the central hole. In Figure 4I, we compared the distribution of the thicknesses of the CuS-iv nanodisks and the Cu_{1.8}S nanorings extracted from large ensembles of AFM topographic heights at the single-pixel level. Due to the increased surface roughness, the distribution of Cu_{1.8}S nanoring thicknesses (excluding the areas where the central hole was located) was significantly broader than that of the CuS-iv nanodisks. Another direct consequence of the covellite-to-digenite phase transition was the decrease of free hole concentrations in the valence band of the materials, which led to weakening and broadening of the plasmon resonance peak in the extinction spectra and downshift of the plasmon resonance frequency deeper into mid-infrared (Figure 4J). Meanwhile, the band gap between HOMO and LUMO also became narrower when covellite

nanodisks were transformed into digenite nanorings. According to the Tauc plots (inset of Figure 4J), the direct band gap value decreased from 2.10 eV for CuS-iv nanodisks to 1.56 eV for the Cu_{1.8}S nanorings.

To gain further insight into the effects of nanodisk thickness, surface topography, and nanodisk stacking on the Fermi-level energy of the Q2D nanoparticles, we correlated the local surface topography to the surface work functions on individual monolithic covellite nanodisks, stacked covellite nanodisks, and digenite nanorings through combined AFM and KPKM measurements. In the KPFM measurements, the nanoparticles were deposited on an ITO substrate, and the contact potential difference (CPD) between the AFM tip and the nanoparticle surface was measured using the ITO substrate as reference. In Figure 5A, we directly compared the topographic heights and the CPDs of an individual CuS-ii nanodisk and a doublelayered nanodisk with two CuS-ii nanodisks stacked on top of each other. Although the stacking of two nanodisks doubled the thickness of the particle, the CPD values remained very similar to those of the single-layer nanodisk. As shown in Figure 5B, the local CPDs also remained unchanged in the regions where two monolithic nanodisks overlapped. Figure 5C shows the correlated AFM and KPFM images of a CuS nanodisk with Moiré patterns (nanodisks synthesized following heating profile 3; see the TEM image in Figure 2C). The Moiré stacking of two monolithic nanodisks did not introduce any significant modifications of the CPDs. Also shown in Figure 5C is a suprastructured particle with three nanodisks stacked together. Although this triple-stacked nanodisk was as thick as ~60 nm, the CPD value was very close to that of the single nanodisk. The CPD values of all CuS nanodisks we measured were always in the range of \sim 8–12 mV, independent of lateral dimensions, nanodisk thicknesses, and how the nanodisks were stacked. As exemplified by multiple materials systems, the stacking of multiple layers of 2D nanomaterials may modify the electronic band structures of the materials, giving rise to the energy shift of the Fermi level, alteration of the band gap values, and even the emergence of peculiar excitonic properties that are unattainable in single-layer 2D materials.46 However, for the CuS nanodisks in the size regime we investigated in this work, the Fermi level was essentially unshifted when multiple monolithic layers were stacked together to form supra-nanostructures.

When the CuS nanodisks transformed into Cu_{1.8}S nanorings, the CPD values increased significantly to \sim 22 mV (Figure 5D) due to the energy shift of the Fermi level caused by the covellite-to-digenite phase transition. We also prepared a sample for AFM/KPFM measurements by depositing a mixture of CuS-v nanodisks and Cu_{1.8}S nanorings on an ITO substrate. We imaged a sample region containing a CuS-v nanodisk with a Cu₁₈S nanoring located nearby (Figure S23 in the Supporting Information). Apparently, the different CPD values of the nanodisk and the nanoring originated from the difference in chemical compositions rather than the thicknesses of the Q2D nanoparticles. Although the multicrystalline Cu_{1.8}S nanoring exhibited roughened surface textures and were rich of grain boundaries, the local CPD values appeared almost uncorrelated to the surface roughness. Figure 5E highlighted the relationship between local CPD and surface topography at the single-pixel level for all CuS-iv nanodisks and Cu_{1.8}S nanorings we measured, and the distributions of CPD values were shown as histograms in Figure 5F. While particle thickness varied significantly from pixel to pixel, the CPD

values were determined primarily by the crystalline phases and compositions of the materials, independent of the local topographic heights of the Q2D nanoparticles.

CONCLUSIONS

Choosing the Cu(II)-thiourea complex as a thermally decomposable single-source precursor, we have developed a temperature-programmed heat-up method that enables us to systematically tune the lateral diameters of the monolithic covellite nanodisks ranging from ~100 to ~300 nm while keeping the nanodisk thicknesses around 11 nm. The expansion of the size-tuning range allows us to tune the plasmon resonances of the covellite nanodisks not only across the entire near-infrared but also deep into mid-infrared. Thicker covellite nanodisks with even larger lateral diameters beyond 300 nm can be synthesized by either increasing the precursor concentrations or using the monolithic nanodisks as seeds to mediate nanodisk overgrowth. These thicker covellite nanodisks are essentially Q2D supra-nanostructures composed of monolithic nanodisks stacked on top of each other, and the overlapping nanodisks are held together by van der Waals interactions. Moiré patterns are clearly observed on individual nanodisks composed of stacked monolithic layers in the TEM images, which are characteristic of superimposed covellite lattices that are horizontally twisted. The monolithic covellite nanodisks further undergo phase transitions under thermal conditions to evolve into multicrystalline digenite nanorings, which not only modifies the plasmonic features but also shifts the Fermi-level and band gap energies of the nanoparticles. Through correlated AFM and KPFM measurements, we have found that for the Q2D copper sulfide nanostructures investigated in this work, their local surface work functions are essentially determined by the crystalline phases and chemical compositions of the materials, almost independent of their local surface topographic features and the layer-bylayer stacking of monolithic units.

ASSOCIATED CONTENT

Supporting Information

The Supporting Information is available free of charge at https://pubs.acs.org/doi/10.1021/acs.chemmater.1c03259.

Additional figures including SEM images, TEM images, EDS results, PXRD patterns, size distributions, Raman spectra, AFM images, and KPFM images as noted in the text (PDF)

AUTHOR INFORMATION

Corresponding Authors

Song Guo — Department of Chemistry and Biochemistry, University of Southern Mississippi, Hattiesburg, Mississippi 39406, United States; orcid.org/0000-0002-3457-4331; Phone: 1-601-266-4702; Email: song.guo@usm.edu

Hui Wang — Department of Chemistry and Biochemistry, University of South Carolina, Columbia, South Carolina 29208, United States; orcid.org/0000-0002-1874-5137; Phone: 1-803-777-2203; Email: wang344@mailbox.sc.edu; Fax: 1-803-777-9521

Authors

Mengqi Sun — Department of Chemistry and Biochemistry, University of South Carolina, Columbia, South Carolina 29208, United States

- Nicholas Kreis Department of Chemistry and Biochemistry, University of Southern Mississippi, Hattiesburg, Mississippi 39406, United States
- Kexun Chen Department of Chemistry and Biochemistry, University of South Carolina, Columbia, South Carolina 29208, United States
- Xiaoqi Fu Department of Chemistry and Biochemistry, University of South Carolina, Columbia, South Carolina 29208, United States; School of Chemistry and Chemical Engineering, Jiangsu University, Zhenjiang, Jiangsu 212013, China; ⁰ orcid.org/0000-0003-1029-4017

Complete contact information is available at: https://pubs.acs.org/10.1021/acs.chemmater.1c03259

Author Contributions

M.S., S.G., and H.W. conceived the idea. M.S. synthesized the nanostructures and characterized the nanostructures using TEM, SEM, HRTEM, PXRD, EDS, and optical extinction spectroscopy. N.K. did the AFM and KPFM measurements. K.C. did the Raman measurements. X.F. conducted the HRTEM measurements. M.S., N.K., S.G., and H.W. analyzed the data. H.W. and S.G. designed the project, supervised the research, and acquired funding support. H.W. and M.S. wrote the paper with contribution from all authors. All authors have given approval to the final version of the manuscript.

Notes

The authors declare no competing financial interest.

ACKNOWLEDGMENTS

The research work conducted at University of South Carolina was supported by the National Science Foundation (NSF) through award OIA-1655740. The work done at the University of Southern Mississippi was supported by the NSF through award DMR-1554841. X.F. acknowledges the Jiangsu University Study-Abroad Funds (20162673) for supporting his visiting scholarship at the University of South Carolina. H.W. acknowledges Jiangsu University for Jinshan Distinguished Professorship (short-term visiting program). This work made use of the X-ray diffraction facilities at the South Carolina SAXS Collaborative supported by the NSF MRI program (DMR-1428620) and the electron microscopy facilities at the University of South Carolina Electron Microscopy Center.

REFERENCES

- (1) Anker, J. N.; Hall, W. P.; Lyandres, O.; Shah, N. C.; Zhao, J.; Van Duyne, R. P. Biosensing with Plasmonic Nanosensors. *Nat. Mater.* **2008**, *7*, 442–453.
- (2) Brongersma, M. L.; Halas, N. J.; Nordlander, P. Plasmon-Induced Hot Carrier Science and Technology. *Nat. Nanotechnol.* **2015**, *10*, 25–34.
- (3) Chen, H.; Shao, L.; Li, Q.; Wang, J. Gold Nanorods and Their Plasmonic Properties. *Chem. Soc. Rev.* **2013**, 42, 2679–2724.
- (4) Eustis, S.; El-Sayed, M. A. Why Gold Nanoparticles Are More Precious Than Pretty Gold: Noble Metal Surface Plasmon Resonance and Its Enhancement of the Radiative and Nonradiative Properties of Nanocrystals of Different Shapes. *Chem. Soc. Rev.* **2006**, *35*, 209–217.
- (5) Halas, N. J.; Lal, S.; Chang, W. S.; Link, S.; Nordlander, P. Plasmons in Strongly Coupled Metallic Nanostructures. *Chem. Rev.* **2011**, *111*, 3913–3961.
- (6) Hu, M.; Chen, J.; Li, Z.-Y.; Au, L.; Hartland, G. V.; Li, X.; Marquez, M.; Xia, Y. Gold Nanostructures: Engineering Their Plasmonic Properties for Biomedical Applications. *Chem. Soc. Rev.* **2006**, *35*, 1084–1094.

- (7) Jain, P. K.; Huang, X. H.; El-Sayed, I. H.; El-Sayed, M. A. Noble Metals on the Nanoscale: Optical and Photothermal Properties and Some Applications in Imaging, Sensing, Biology, and Medicine. *Acc. Chem. Res.* **2008**, *41*, 1578–1586.
- (8) Murphy, C. J.; San, T. K.; Gole, A. M.; Orendorff, C. J.; Gao, J.; Gou, L.; Hunyadi, S. E.; Li, T. Anisotropic Metal Nanoparticles: Synthesis, Assembly, and Optical Applications. *J. Phys. Chem. B* **2005**, *109*, 13857–13870.
- (9) Naik, G. V.; Shalaev, V. M.; Boltasseva, A. Alternative Plasmonic Materials: Beyond Gold and Silver. *Adv. Mater.* **2013**, *25*, 3264–3294.
- (10) West, P. R.; Ishii, S.; Naik, G. V.; Emani, N. K.; Shalaev, V. M.; Boltasseva, A. Searching for Better Plasmonic Materials. *Laser Photon. Rev.* **2010**, *4*, 795–808.
- (11) Comin, A.; Manna, L. New Materials for Tunable Plasmonic Colloidal Nanocrystals. *Chem. Soc. Rev.* **2014**, *43*, 3957–3975.
- (12) Manthiram, K.; Alivisatos, A. P. Tunable Localized Surface Plasmon Resonances in Tungsten Oxide Nanocrystals. *J. Am. Chem. Soc.* **2012**, *134*, 3995–3998.
- (13) Ye, X.; Fei, J.; Diroll, B. T.; Paik, T.; Murray, C. B. Expanding the Spectral Tunability of Plasmonic Resonances in Doped Metal-Oxide Nanocrystals through Cooperative Cation-Anion Codoping. *J. Am. Chem. Soc.* **2014**, *136*, 11680–11686.
- (14) Buonsanti, R.; Llordes, A.; Aloni, S.; Helms, B. A.; Milliron, D. J. Tunable Infrared Absorption and Visible Transparency of Colloidal Aluminum-Doped Zinc Oxide Nanocrystals. *Nano Lett.* **2011**, *11*, 4706–4710.
- (15) Kanehara, M.; Koike, H.; Yoshinaga, T.; Teranishi, T. Indium Tin Oxide Nanoparticles with Compositionally Tunable Surface Plasmon Resonance Frequencies in the Near-IR Region. *J. Am. Chem. Soc.* **2009**, *131*, 17736–17737.
- (16) Lounis, S. D.; Runnerstrom, E. L.; Bergerud, A.; Nordlund, D.; Milliron, D. J. Influence of Dopant Distribution on the Plasmonic Properties of Indium Tin Oxide Nanocrystals. *J. Am. Chem. Soc.* **2014**, 136, 7110–7116.
- (17) Gordon, T. R.; Paik, T.; Klein, D. R.; Naik, G. V.; Caglayan, H.; Boltasseva, A.; Murray, C. B. Shape-Dependent Plasmonic Response and Directed Self-Assembly in a New Semiconductor Building Block, Indium-Doped Cadmium Oxide (ICO). *Nano Lett.* **2013**, *13*, 2857–2863.
- (18) Liu, Z.; Zhong, Y.; Shafei, I.; Jeong, S.; Wang, L.; Nguyen, H. T.; Sun, C.-J.; Li, T.; Chen, J.; Chen, L.; Losovyj, Y.; Gao, X.; Ma, W.; Ye, X. Broadband Tunable Mid-Infrared Plasmon Resonances in Cadmium Oxide Nanocrystals Induced by Size-Dependent Nonstoichiometry. *Nano Lett.* **2020**, *20*, 2821–2828.
- (19) Zhao, Y.; Pan, H.; Lou, Y.; Qiu, X.; Zhu, J.; Burda, C. Plasmonic Cu_{2-X}S Nanocrystals: Optical and Structural Properties of Copper-Deficient Copper(I) Sulfides. *J. Am. Chem. Soc.* **2009**, *131*, 4253–4261.
- (20) Luther, J. M.; Jain, P. K.; Ewers, T.; Alivisatos, A. P. Localized Surface Plasmon Resonances Arising from Free Carriers in Doped Quantum Dots. *Nat. Mater.* **2011**, *10*, 361–366.
- (21) Dorfs, D.; Härtling, T.; Miszta, K.; Bigall, N. C.; Kim, M. R.; Genovese, A.; Falqui, A.; Povia, M.; Manna, L. Reversible Tunability of the near-Infrared Valence Band Plasmon Resonance in $Cu_{2-X}Se$ Nanocrystals. *J. Am. Chem. Soc.* **2011**, *133*, 11175–11180.
- (22) Hsu, S.-W.; On, K.; Tao, A. R. Localized Surface Plasmon Resonances of Anisotropic Semiconductor Nanocrystals. *J. Am. Chem. Soc.* **2011**, *133*, 19072–19075.
- (23) Kriegel, I.; Jiang, C.; Rodríguez-Fernández, J.; Schaller, R. D.; Talapin, D. V.; da Como, E.; Feldmann, J. Tuning the Excitonic and Plasmonic Properties of Copper Chalcogenide Nanocrystals. *J. Am. Chem. Soc.* **2012**, *134*, 1583–1590.
- (24) Xie, Y.; Riedinger, A.; Prato, M.; Casu, A.; Genovese, A.; Guardia, P.; Sottini, S.; Sangregorio, C.; Miszta, K.; Ghosh, S.; Pellegrino, T.; Manna, L. Copper Sulfide Nanocrystals with Tunable Composition by Reduction of Covellite Nanocrystals with Cu⁺ Ions. *J. Am. Chem. Soc.* **2013**, *135*, 17630–17637.
- (25) Kriegel, I.; Rodríguez-Fernández, J.; Wisnet, A.; Zhang, H.; Waurisch, C.; Eychmüller, A.; Dubavik, A.; Govorov, A. O.;

- Feldmann, J. Shedding Light on Vacancy-Doped Copper Chalcogenides: Shape-Controlled Synthesis, Optical Properties, and Modeling of Copper Telluride Nanocrystals with near-Infrared Plasmon Resonances. ACS Nano 2013, 7, 4367—4377.
- (26) Liu, X.; Wang, X.; Swihart, M. T. $Cu_{2-x}S_{1-y}Se_y$ Alloy Nanocrystals with Broadly Tunable near-Infrared Localized Surface Plasmon Resonance. *Chem. Mater.* **2013**, *25*, 4402–4408.
- (27) Hsu, S.-W.; Ngo, C.; Tao, A. R. Tunable and Directional Plasmonic Coupling within Semiconductor Nanodisk Assemblies. *Nano Lett.* **2014**, *14*, 2372–2380.
- (28) Liu, Y.; Liu, M.; Swihart, M. T. Plasmonic Copper Sulfide-Based Materials: A Brief Introduction to Their Synthesis, Doping, Alloying, and Applications. *J. Phys. Chem. C* **2017**, *121*, 13435–13447.
- (29) Liu, X.; Law, W.-C.; Jeon, M.; Wang, X.; Liu, M.; Kim, C.; Prasad, P. N.; Swihart, M. T. Cu_{2-X}Se Nanocrystals with Localized Surface Plasmon Resonance as Sensitive Contrast Agents for in Vivo Photoacoustic Imaging: Demonstration of Sentinel Lymph Node Mapping. *Adv. Healthcare Mater.* **2013**, 2, 952–957.
- (30) Liu, Y.; Liu, M.; Swihart, M. T. Reversible Crystal Phase Interconversion between Covellite Cus and High Chalcocite Cu₂S Nanocrystals. *Chem. Mater.* **2017**, *29*, 4783–4791.
- (31) Manna, G.; Bose, R.; Pradhan, N. Semiconducting and Plasmonic Copper Phosphide Platelets. *Angew. Chem., Int. Ed.* **2013**, 52, 6762–6766.
- (32) De Trizio, L.; Gaspari, R.; Bertoni, G.; Kriegel, I.; Moretti, L.; Scotognella, F.; Maserati, L.; Zhang, Y.; Messina, G. C.; Prato, M.; Marras, S.; Cavalli, A.; Manna, L. Cu_{3-X}P Nanocrystals as a Material Platform for near-Infrared Plasmonics and Cation Exchange Reactions. *Chem. Mater.* **2015**, *27*, 1120–1128.
- (33) Palomaki, P. K. B.; Miller, E. M.; Neale, N. R. Control of Plasmonic and Interband Transitions in Colloidal Indium Nitride Nanocrystals. *J. Am. Chem. Soc.* **2013**, *135*, 14142–14150.
- (34) Askari, S.; Mariotti, D.; Stehr, J. E.; Benedikt, J.; Keraudy, J.; Helmersson, U. Low-Loss and Tunable Localized Mid-Infrared Plasmons in Nanocrystals of Highly Degenerate InN. *Nano Lett.* **2018**, *18*, 5681–5687.
- (35) Agrawal, A.; Cho, S. H.; Zandi, O.; Ghosh, S.; Johns, R. W.; Milliron, D. J. Localized Surface Plasmon Resonance in Semi-conductor Nanocrystals. *Chem. Rev.* **2018**, *118*, 3121–3207.
- (36) Faucheaux, J. A.; Stanton, A. L. D.; Jain, P. K. Plasmon Resonances of Semiconductor Nanocrystals: Physical Principles and New Opportunities. *J. Phys. Chem. Lett.* **2014**, *5*, 976–985.
- (37) Liu, X.; Swihart, M. T. Heavily-Doped Colloidal Semiconductor and Metal Oxide Nanocrystals: An Emerging New Class of Plasmonic Nanomaterials. *Chem. Soc. Rev.* **2014**, *43*, 3908–3920.
- (38) Coughlan, C.; Ibanez, M.; Dobrozhan, O.; Singh, A.; Cabot, A.; Ryan, K. M. Compound Copper Chalcogenide Nanocrystals. *Chem. Rev.* **2017**, *117*, 5865–6109.
- (39) Chen, L.; Hu, H.; Chen, Y.; Gao, J.; Li, G. Plasmonic Cu_{2-X}S Nanoparticles: A Brief Introduction of Optical Properties and Applications. *Mater. Adv.* **2021**, *2*, 907–926.
- (40) Xie, Y.; Carbone, L.; Nobile, C.; Grillo, V.; D'Agostino, S.; Della Sala, F.; Giannini, C.; Altamura, D.; Oelsner, C.; Kryschi, C.; Cozzoli, P. D. Metallic-Like Stoichiometric Copper Sulfide Nanocrystals: Phase- and Shape-Selective Synthesis, near-Infrared Surface Plasmon Resonance Properties, and Their Modeling. ACS Nano 2013, 7, 7352–7369.
- (41) van der Stam, W.; Gudjonsdottir, S.; Evers, W. H.; Houtepen, A. J. Switching between Plasmonic and Fluorescent Copper Sulfide Nanocrystals. *J. Am. Chem. Soc.* **2017**, *139*, 13208–13217.
- (42) Córdova-Castro, R. M.; Casavola, M.; van Schilfgaarde, M.; Krasavin, A. V.; Green, M. A.; Richards, D.; Zayats, A. V. Anisotropic Plasmonic CuS Nanocrystals as a Natural Electronic Material with Hyperbolic Optical Dispersion. *ACS Nano* **2019**, *13*, 6550–6560.
- (43) Izquierdo, E.; Robin, A.; Keuleyan, S.; Lequeux, N.; Lhuillier, E.; Ithurria, S. Strongly Confined HgTe 2D Nanoplatelets as Narrow near-Infrared Emitters. *J. Am. Chem. Soc.* **2016**, *138*, 10496–10501.

- (44) Pedetti, S.; Ithurria, S.; Heuclin, H.; Patriarche, G.; Dubertret, B. Type-II CdSe/CdTe Core/Crown Semiconductor Nanoplatelets. *J. Am. Chem. Soc.* **2014**, *136*, 16430–16438.
- (45) Wong, A. B.; Bekenstein, Y.; Kang, J.; Kley, C. S.; Kim, D.; Gibson, N. A.; Zhang, D.; Yu, Y.; Leone, S. R.; Wang, L.-W.; Alivisatos, A. P.; Yang, P. Strongly Quantum Confined Colloidal Cesium Tin Iodide Perovskite Nanoplates: Lessons for Reducing Defect Density and Improving Stability. *Nano Lett.* **2018**, *18*, 2060–2066.
- (46) He, F.; Zhou, Y.; Ye, Z.; Cho, S.-H.; Jeong, J.; Meng, X.; Wang, Y. Moire Patterns in 2d Materials: A Review. ACS Nano 2021, 15, 5944-5958.
- (47) Xiao, Y.; Liu, J.; Fu, L. Moire Is More: Access to New Properties of Two-Dimensional Layered Materials. *Matter* **2020**, 3, 1142–1161.
- (48) Wang, D.-D.; Gong, X.-G.; Yang, J.-H. Unusual Interlayer Coupling in Layered Cu-Based Ternary Chalcogenides Cumch₂ (M = Sb, Bi; Ch = S, Se). *Nanoscale* **2021**, *13*, 14621–14627.
- (49) Palummo, M.; Bernardi, M.; Grossman, J. C. Exciton Radiative Lifetimes in Two-Dimensional Transition Metal Dichalcogenides. *Nano Lett.* **2015**, *15*, 2794–2800.
- (50) Alexeev, E. M.; Ruiz-Tijerina, D. A.; Danovich, M.; Hamer, M. J.; Terry, D. J.; Nayak, P. K.; Ahn, S.; Pak, S.; Lee, J.; Sohn, J. I.; Molas, M. R.; Koperski, M.; Watanabe, K.; Taniguchi, T.; Novoselov, K. S.; Gorbachev, R. V.; Shin, H. S.; Fal'ko, V. I.; Tartakovskii, A. I. Resonantly Hybridized Excitons in Moire Superlattices in van der Waals Heterostructures. *Nature* 2019, 567, 81–86.
- (51) Brown, L.; Hovden, R.; Huang, P.; Wojcik, M.; Muller, D. A.; Park, J. Twinning and Twisting of Tri- and Bilayer Graphene. *Nano Lett.* **2012**, *12*, 1609–1615.
- (52) Fang, H.; Battaglia, C.; Carraro, C.; Nemsak, S.; Ozdol, B.; Kang, J. S.; Bechtel, H. A.; Desai, S. B.; Kronast, F.; Unal, A. A.; Conti, G.; Conlon, C.; Palsson, G. K.; Martin, M. C.; Minor, A. M.; Fadley, C. S.; Yablonovitch, E.; Maboudian, R.; Javey, A. Strong Interlayer Coupling in van der Waals Heterostructures Built from Single-Layer Chalcogenides. *Proc. Natl. Acad. Sci. U. S. A.* **2014**, *111*, 6198–6202.
- (53) Millstone, J. E.; Hurst, S. J.; Métraux, G. S.; Cutler, J. I.; Mirkin, C. A. Colloidal Gold and Silver Triangular Nanoprisms. *Small* **2009**, 5, 646–664.
- (54) Zhang, Q.; Hu, Y.; Guo, S.; Goebl, J.; Yin, Y. Seeded Growth of Uniform Ag Nanoplates with High Aspect Ratio and Widely Tunable Surface Plasmon Bands. *Nano Lett.* **2010**, *10*, 5037–5042.
- (55) Pastoriza-Santos, I.; Liz-Marzan, L. M. Colloidal Silver Nanoplates. State of the Art and Future Challenges. *J. Mater. Chem.* **2008**, *18*, 1724–1737.
- (56) Zhang, H. T.; Wu, G.; Chen, X. H. Controlled Synthesis and Characterization of Covellite (CuS) Nanoflakes. *Mater. Chem. Phys.* **2006**, *98*, 298–303.
- (57) Hsu, S. W.; Ngo, C.; Bryks, W.; Tao, A. R. Shape Focusing During the Anisotropic Growth of CuS Triangular Nanoprisms. *Chem. Mater.* **2015**, 27, 4957–4963.
- (58) Saldanha, P. L.; Brescia, R.; Prato, M.; Li, H.; Povia, M.; Manna, L.; Lesnyak, V. Generalized One-Pot Synthesis of Copper Sulfide, Selenide-Sulfide, and Telluride-Sulfide Nanoparticles. *Chem. Mater.* **2014**, *26*, 1442–1449.
- (59) Ghezelbash, A.; Korgel, B. A. Nickel Sulfide and Copper Sulfide Nanocrystal Synthesis and Polymorphism. *Langmuir* **2005**, *21*, 9451–9456.
- (60) Du, Y.; Yin, Z.; Zhu, J.; Huang, X.; Wu, X.-J.; Zeng, Z.; Yan, Q.; Zhang, H. A General Method for the Large-Scale Synthesis of Uniform Ultrathin Metal Sulphide Nanocrystals. *Nat. Commun.* **2012**, 3, 1177.
- (61) Zhang, H.; Zhang, Y.; Yu, J.; Yang, D. Phase-Selective Synthesis and Self-Assembly of Monodisperse Copper Sulfide Nanocrystals. *J. Phys. Chem. C* **2008**, *112*, 13390–13394.
- (62) Bryks, W.; Lupi, E.; Ngo, C.; Tao, A. R. Digenite Nanosheets Synthesized by Thermolysis of Layered Copper-Alkanethiolate Frameworks. J. Am. Chem. Soc. 2016, 138, 13717–13725.

- (63) Du, X.-S.; Mo, M.; Zheng, R.; Lim, S.-H.; Meng, Y.; Mai, Y.-W. Shape-Controlled Synthesis and Assembly of Copper Sulfide Nanoparticles. *Cryst. Growth Des.* **2008**, *8*, 2032–2035.
- (64) Lim, W. P.; Wong, C. T.; Ang, S. L.; Low, H. Y.; Chin, W. S. Phase-Selective Synthesis of Copper Sulfide Nanocrystals. *Chem. Mater.* **2006**, *18*, 6170–6177.
- (65) Lou, W.; Chen, M.; Wang, X.; Liu, W. Size Control of Monodisperse Copper Sulfide Faceted Nanocrystals and Triangular Nanoplates. *J. Phys. Chem. C* **2007**, *111*, 9658–9663.
- (66) Tian, Q.; Jiang, F.; Zou, R.; Liu, Q.; Chen, Z.; Zhu, M.; Yang, S.; Wang, J.; Wang, J.; Hu, J. Hydrophilic Cu₉S₅ Nanocrystals: A Photothermal Agent with a 25.7% Heat Conversion Efficiency for Photothermal Ablation of Cancer Cells *in Vivo. ACS Nano* **2011**, *5*, 9761–9771.
- (67) Morales-Garcia, A.; Soares, A. L., Jr.; Dos Santos, E. C.; de Abreu, H. A.; Duarte, H. A. First-Principles Calculations and Electron Density Topological Analysis of Covellite (CuS). *J. Phys. Chem. A* **2014**, *118*, 5823–5831.
- (68) Sánchez-Iglesias, A.; Winckelmans, N.; Altantzis, T.; Bals, S.; Grzelczak, M.; Liz-Márzan, L. M. High-Yield Seeded Growth of Monodisperse Pentatwinned Gold Nanoparticles through Thermally Induced Seed Twinning. J. Am. Chem. Soc. 2017, 139, 107–110.
- (69) Millstone, J. E.; Wei, W.; Jones, M. R.; Yoo, H.; Mirkin, C. A. Iodide Ions Control Seed-Mediated Growth of Anisotropic Gold Nanoparticles. *Nano Lett.* **2008**, *8*, 2526–2529.
- (70) Walsh, M. J.; Tong, W.; Katz-Boon, H.; Mulvaney, P.; Etheridge, J.; Funston, A. M. A Mechanism for Symmetry Breaking and Shape Control in Single-Crystal Gold Nanorods. *Acc. Chem. Res.* **2017**, *50*, 2925–2935.
- (71) Walsh, M. J.; Barrow, S. J.; Tong, W.; Funston, A. M.; Etheridge, J. Symmetry Breaking and Silver in Gold Nanorod Growth. *ACS Nano* **2015**, *9*, 715–724.
- (72) Zhang, Y. Q.; Zhang, B. P.; Zhu, L. F. Monodisperse Cus Nanodisks: Low-Temperature Solvothermal Synthesis and Enhanced Photocatalytic Activity. *RSC Adv.* **2014**, *4*, 59185–59193.
- (73) Kumar, P.; Gusain, M.; Nagarajan, R. Synthesis of Cu_{1.8}S and CuS from Copper-Thiourea Containing Precursors; Anionic (Cl⁻, NO₃⁻, SO₄²⁻) Influence on the Product Stoichiometry. *Inorg. Chem.* **2011**, *50*, 3065–3070.
- (74) Liu, M.; Xue, X.; Ghosh, C.; Liu, X.; Liu, Y.; Furlani, E. P.; Swihart, M. T.; Prasad, P. N. Room-Temperature Synthesis of Covellite Nanoplatelets with Broadly Tunable Localized Surface Plasmon Resonance. *Chem. Mater.* **2015**, *27*, 2584–2590.
- (75) Adhikari, S.; Sarkar, D.; Madras, G. Hierarchical Design of CuS Architectures for Visible Light Photocatalysis of 4-Chlorophenol. *ACS Omega* **2017**, *2*, 4009–4021.
- (76) Kundu, J.; Pradhan, D. Influence of Precursor Concentration, Surfactant and Temperature on the Hydrothermal Synthesis of CuS: Structural, Thermal and Optical Properties. *New J. Chem.* **2013**, *37*, 1470–1478.
- (77) Basu, M.; Sinha, A. K.; Pradhan, M.; Sarkar, S.; Negishi, Y.; Govind; Pal, T. Evolution of Hierarchical Hexagonal Stacked Plates of CuS from Liquid-Liquid Interface and Its Photocatalytic Application for Oxidative Degradation of Different Dyes under Indoor Lighting. *Environ. Sci. Technol.* **2010**, *44*, 6313–6318.
- (78) Ward, A. T. Raman Spectroscopy of Sulfur Sulfur-Selenium and Sulfur-Arsenic Mixtures. J. Phys. Chem. 1968, 72, 4133–4139.
- (79) Skrabalak, S. E.; Wiley, B. J.; Kim, M.; Formo, E. V.; Xia, Y. On the Polyol Synthesis of Silver Nanostructures: Glycolaldehyde as a Reducing Agent. *Nano Lett.* **2008**, *8*, 2077–2081.
- (80) Li, G. G.; Wang, Z.; Blom, D. A.; Wang, H. Tweaking the Interplay among Galvanic Exchange, Oxidative Etching, and Seed-Mediated Deposition toward Architectural Control of Multimetallic Nanoelectrocatalysts. ACS Appl. Mater. Interfaces 2019, 11, 23482—23494.

Supporting Information for

Covellite Nanodisks and Digenite Nanorings: Colloidal

Synthesis, Phase Transitions, and Optical Properties

Mengqi Sun,[†] Nicholas Kreis,[‡] Kexun Chen,[†] Xiaoqi Fu,^{†,§} Song Guo, *,[‡] and Hui Wang*,[†]

† Department of Chemistry and Biochemistry, University of South Carolina, Columbia, South

Carolina 29208, United States

[‡] Department of Chemistry and Biochemistry, University of Southern Mississippi, Hattiesburg,

Mississippi 39406, United States

§ School of Chemistry and Chemical Engineering, Jiangsu University, Zhenjiang, Jiangsu 212013,

China.

* To whom correspondence should be addressed.

Email: wang344@mailbox.sc.edu (H. Wang)

Email: song.guo@usm.edu (S. Guo)

1

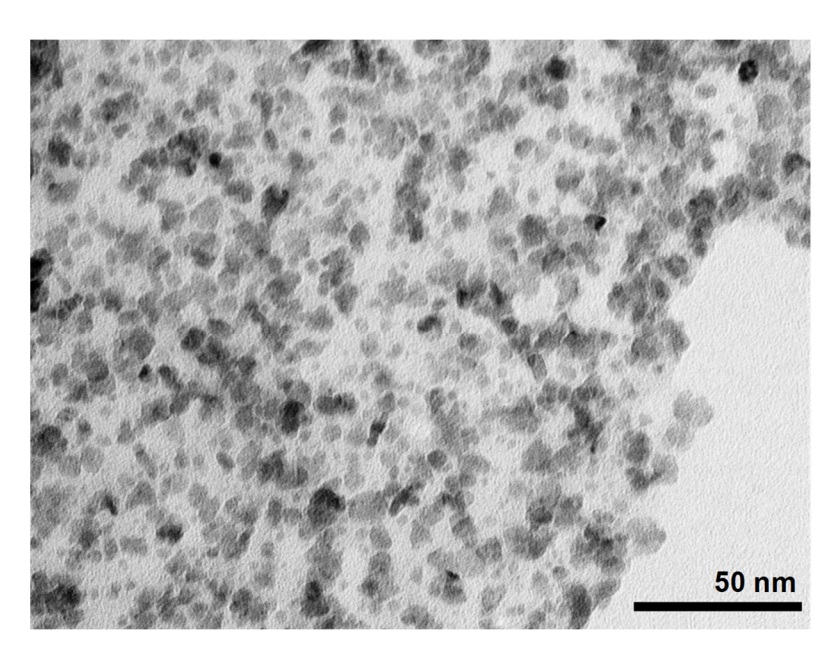


Figure S1. TEM image of CuS nuclei formed at a reaction time of 300 min during the temperature-programmed heat-up process. The heating profile was shown in Figure 1B.

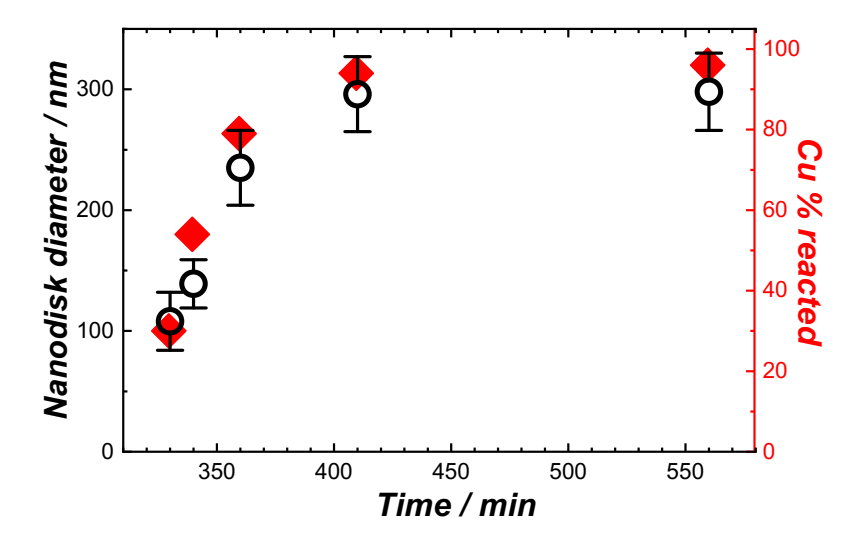


Figure S2. Temporal evolution of the lateral diameters of the nanodisks (black open circles) and percentage of Cu reacted (solid red diamonds) during the nanodisk growth at various reaction times in the temperature-programmed heat-up process. The lateral diameters of various nanodisk samples were determined by TEM and the percentages of reacted Cu were calculated by normalizing the Cu mass in the nanodisks (quantified by ICP-MS) against the total Cu mass in the precursors.

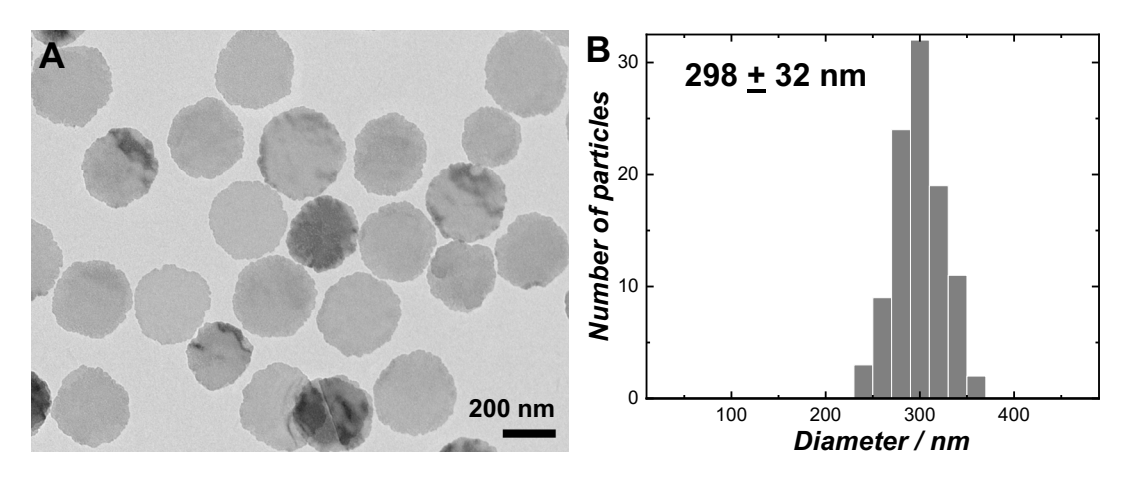


Figure S3. (A) TEM image and (B) size distribution histograms of CuS nanodisks produced after maintaining the reaction temperature at 130 °C for 200 min.

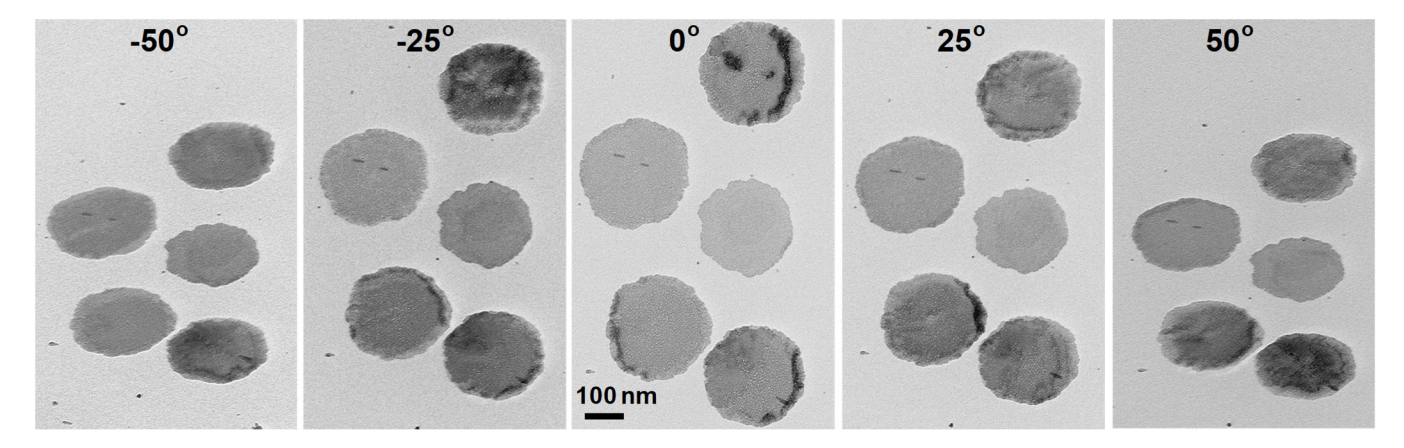


Figure S4. Tilted TEM images of CuS-iv nanodisks. The tilt angles with respect to the normal projection are labeled at the top of each image.

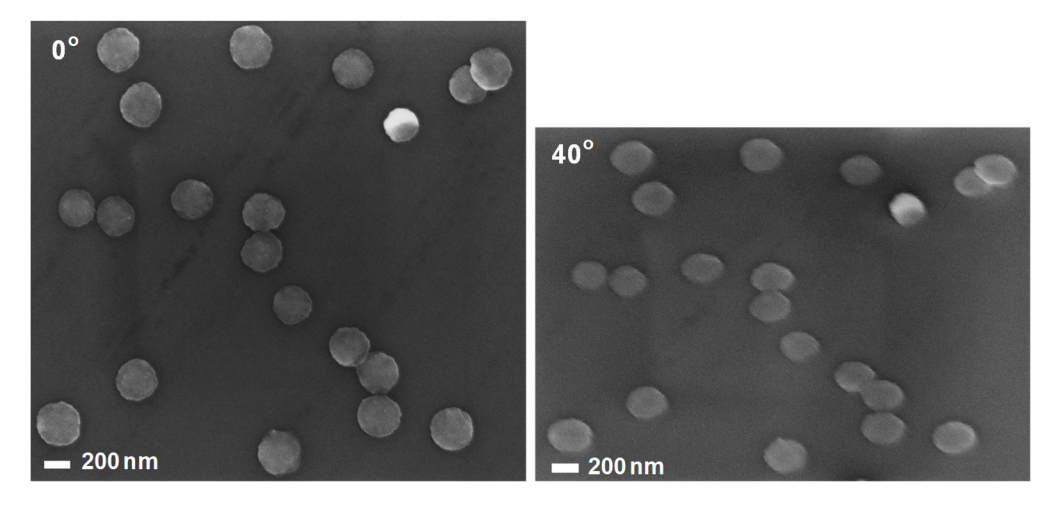


Figure S5. SEM images of CuS-iv nanodisks viewed at the normal projection and at a tilt angle of 40° with respect to the normal projection.

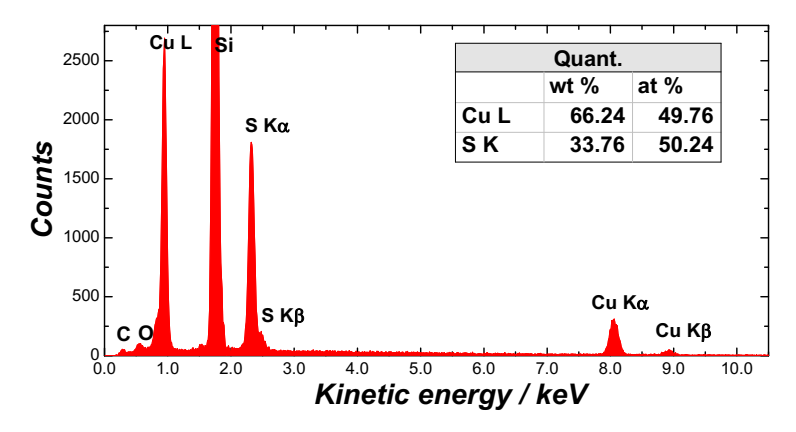


Figure S6. EDS spectrum of CuS-iv nanodisks. The weight and atomic percentages of Cu and S were quantified based on the intensities of the Cu L and S K lines, respectively. The peak centered at 1.75 keV was the signals from the Si substrate.

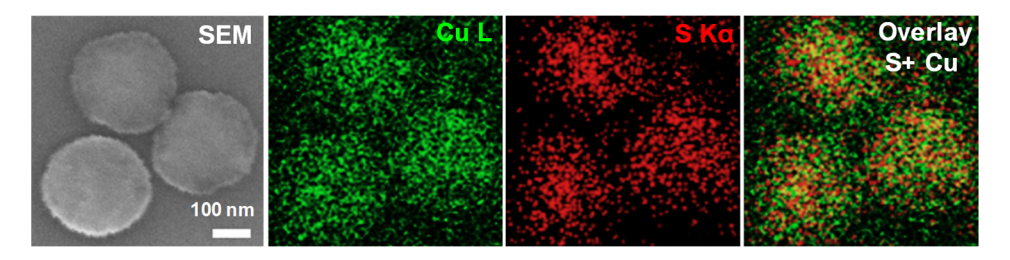


Figure S7. SEM image and EDS elemental maps of CuS-iv nanodisks.

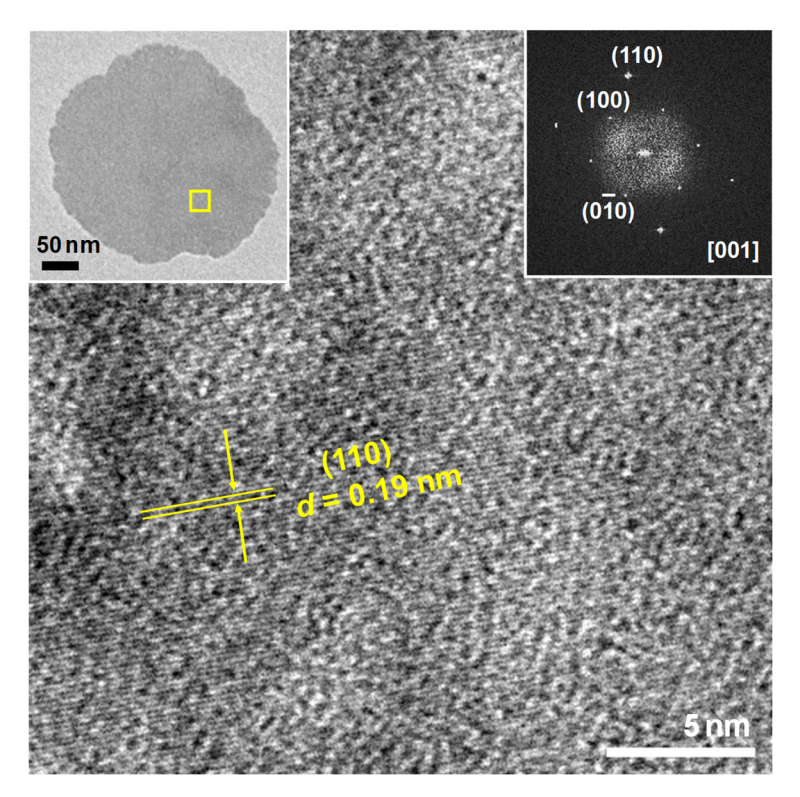


Figure S8. HRTEM image of a selected region within a CuS-iv nanodisk. The TEM image of the entire nanodisk and the fast Fourier transform (FFT) pattern of the HRTEM image were shown in the upper-left and upper-right insets, respectively.

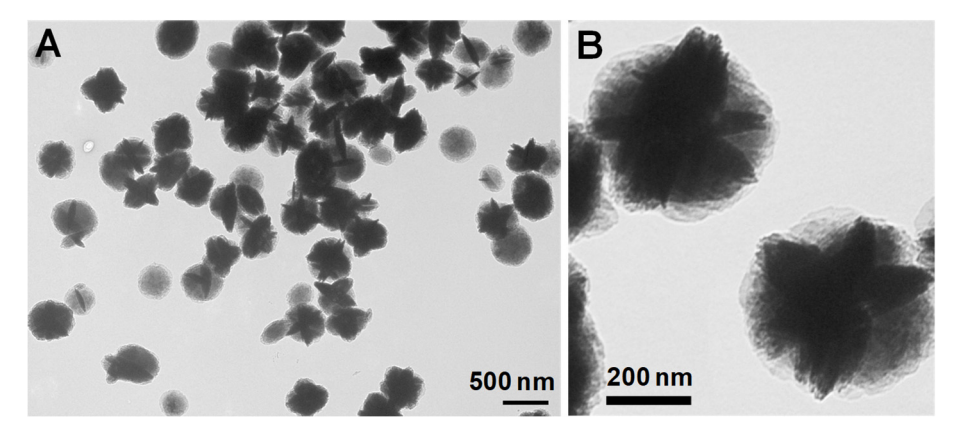


Figure S9. TEM images of CuS nanoparticles synthesized in the absence of PVP. The image in panel A was taken with a lower magnification than the one in panel B. The detailed protocol for the synthesis of this sample is described as follows: 0.4 mL of 0.1 M Cu(NO₃)₂ and 1.6 mL of 0.1 M thiourea were added to 8 mL EG at room temperature. The solution was kept in a temperature-controlled heating mantle following the programmed Heating Profile 1 (shown in Figure 2A). The produced colloidal particles were rapidly cooled down in an ice bath and separated from the reactant mixtures through centrifugation-redispersion cycles with ethanol and were finally stored in ethanol.

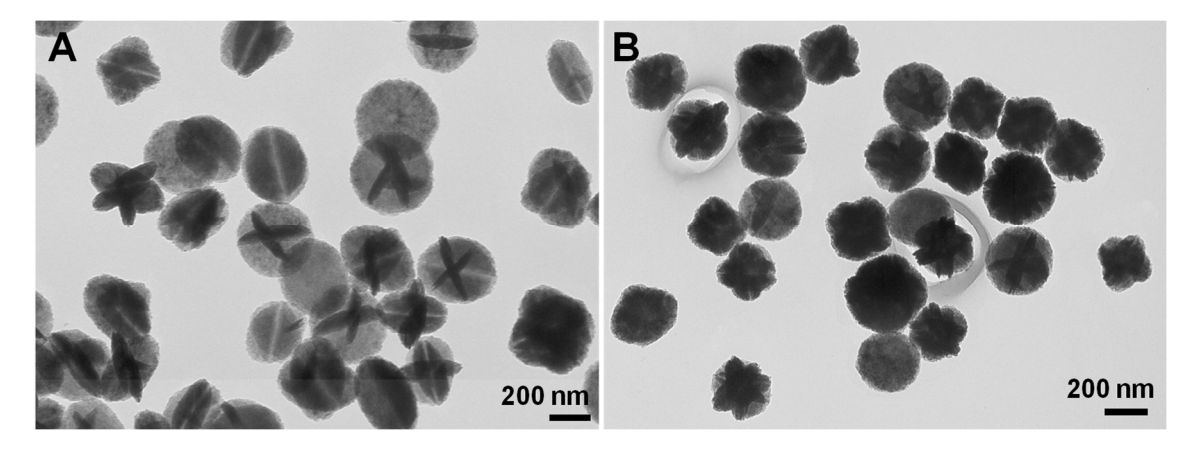


Figure S10. TEM images of CuS nanoparticles synthesized under magnetic stir at different speeds. The detailed protocol for the synthesis of these samples is described as follows: 0.1 g of PVP was first dissolved in 8 mL of EG. Then 0.4 mL of 0.1 M Cu(NO₃)₂ and 1.6 mL of 0.1 M thiourea were added to the EG solution of PVP at room temperature. The reactant mixtures were kept under magnetic stir at fixed speeds (100 rpm for the sample in panel A and 300 rpm for the sample in panel B, respectively) in a temperature-controlled heating mantle following the programmed Heating Profile 1 (shown in Figure 2A). The produced colloidal particles were rapidly cooled down in an ice bath and separated from the reactant mixtures through centrifugation-redispersion cycles and were finally stored in ethanol.

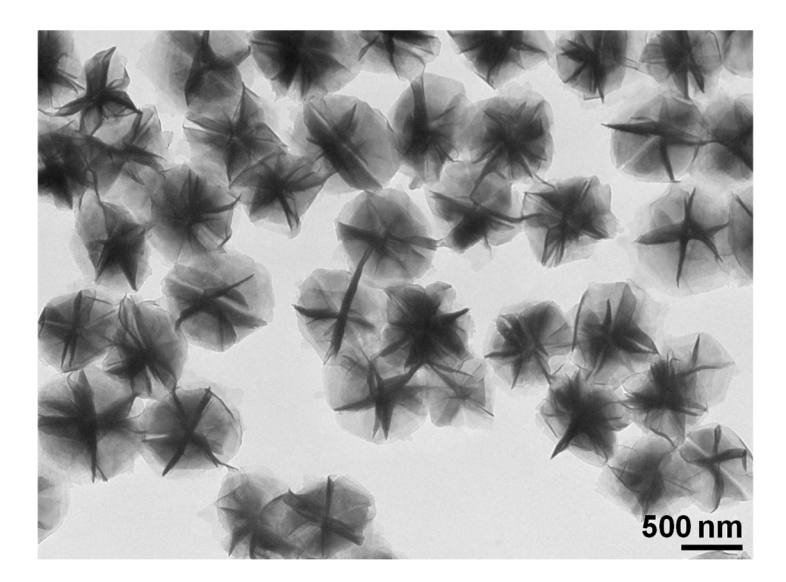


Figure S11. TEM image of CuS nanoparticles synthesized under magnetic stir at 300 rpm in the presence of 0.06 g mL⁻¹ PVP. The detailed protocol for the synthesis of this sample is described as follows: 0.4 mL of 0.1 M Cu(NO₃)₂, 1.6 mL of 0.1 M thiourea, and 0.6 g of PVP were added to 8 mL EG at room temperature. The reactant mixtures were kept under magnetic stir at 300 rpm in a temperature-controlled heating mantle following the programmed Heating Profile 1 (shown in Figure 2A). The produced colloidal particles were rapidly cooled down in an ice bath and separated from the reactant mixtures through centrifugation-redispersion cycles and were finally stored in ethanol.

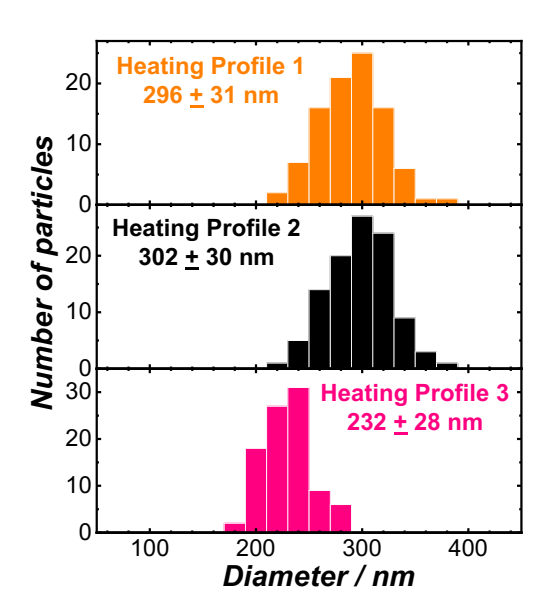


Figure S12. Distributions of the lateral diameters of CuS nanodisks synthesized through programmed (*top panel*) Heating Profile 1, (*middle panel*) Heating Profile 2, and (*bottom panel*) Heating Profile 3. The size distributions were obtained through analysis of more than 100 nanodisks in the TEM images of each sample. The precursor mixture solutions for these three samples were prepared in exactly the same way by adding 0.1 g PVP, 0.4 mL of 0.1 M Cu(NO₃)₂, and 1.6 mL of 0.1 M thiourea to 8 mL EG.

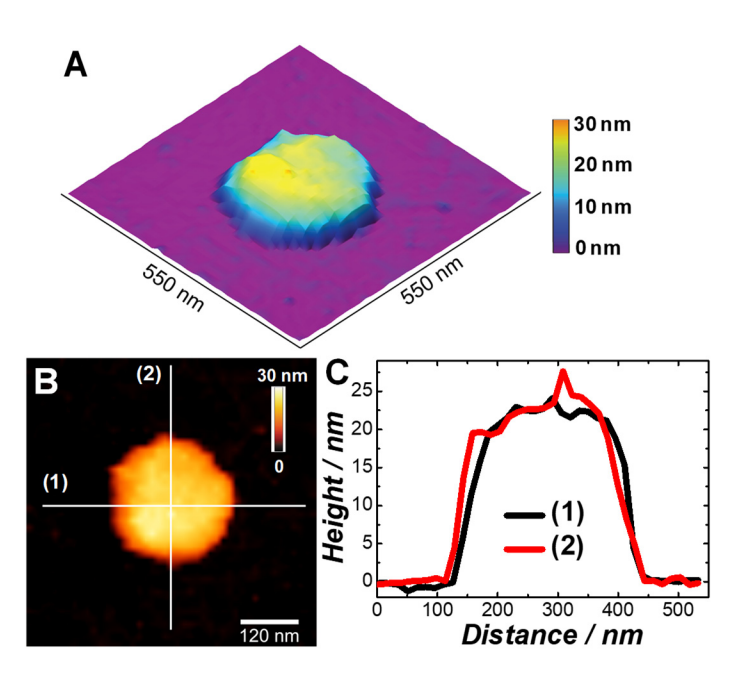


Figure S13. (A) 3D and (B) 2D representations of an AFM topographic image of an individual CuS nanodisk synthesized following the temperature-programmed Heating Profile 3. (C) Topographic height profiles along the line (1) and line (2) in panel B.

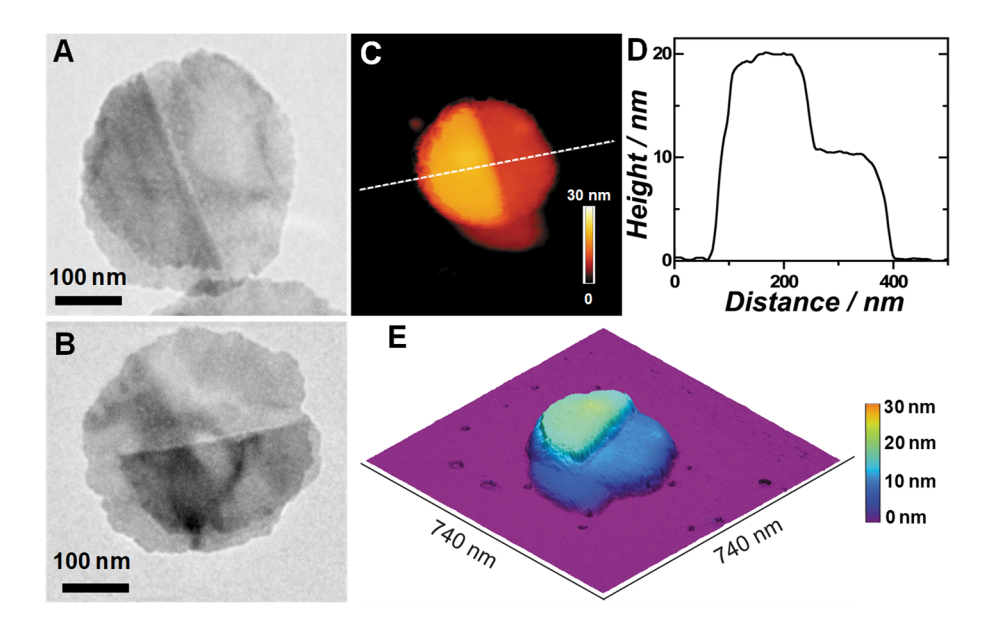


Figure S14. (A, B) TEM images of individual double-stacked nanodisks in the CuS-v sample. (C) 2D representation of AFM topographic image, (D) topographic height profiles along the dash line in panel C, and (E) 3D representation of AFM topographic image of an individual nanodisk consisting of a semicircle-shaped half nanodisk staked on top of a nanodisk.

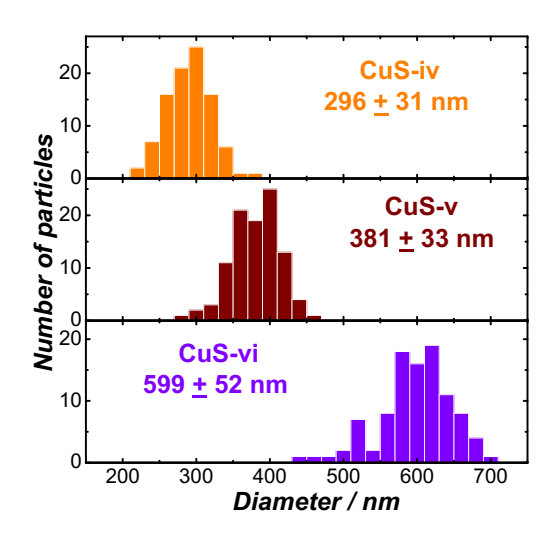


Figure S15. Distributions of the lateral diameters of (*top panel*) CuS-iv, (*middle panel*) CuS-v, and (*bottom panel*) CuS-vi nanodisks. The size distributions were obtained through analysis of more than 100 nanodisks in the TEM images of each sample.

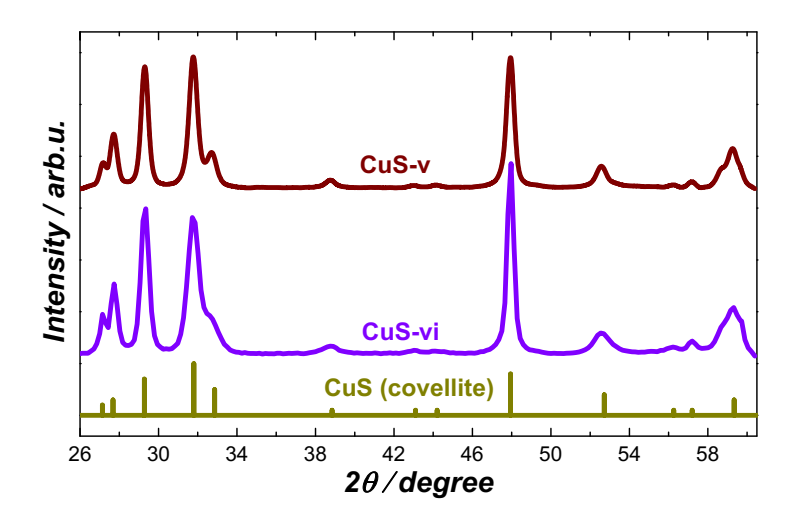


Figure S16. PXRD patterns of CuS-v and CuS-vi nanodisks. Standard pattern of CuS (covellite, JCPDS 6-464) was shown as the reference for comparison.

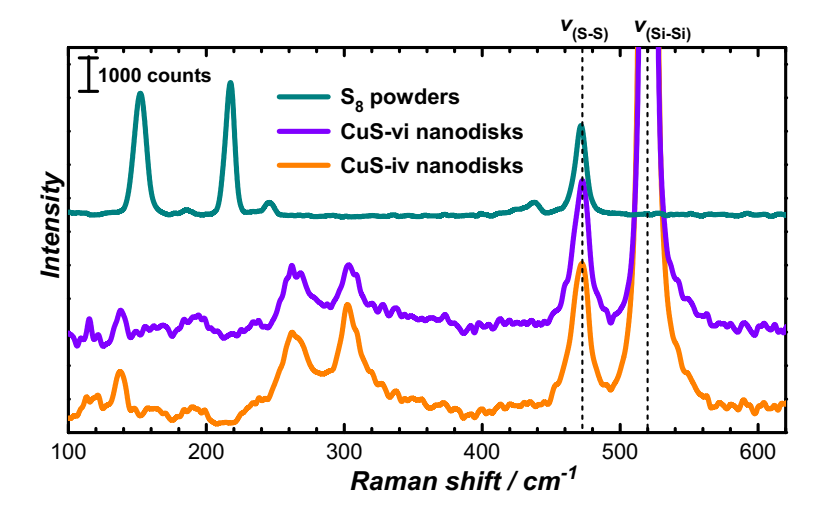


Figure S17. Raman spectra of sulfur powders, CuS-vi nanodisks, and CuS-iv nanodisks. The excitation wavelength was 785 nm and the power of the excitation laser focused on the samples was 5.0 mW. The spectral integration time was 30 s. The nanodisks were dispersed on Si substrates. The characteristic peaks of the S-S bond and Si-Si bond stretching modes were centered at 472 and 520 cm⁻¹, respectively.

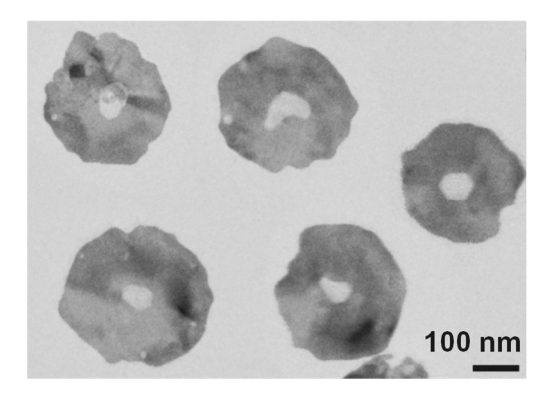


Figure S18. TEM image of digenite nanorings obtained after maintaining the temperature of colloidal suspensions of CuS-iv nanodisks (in TEG) at 180 °C for 120 min.

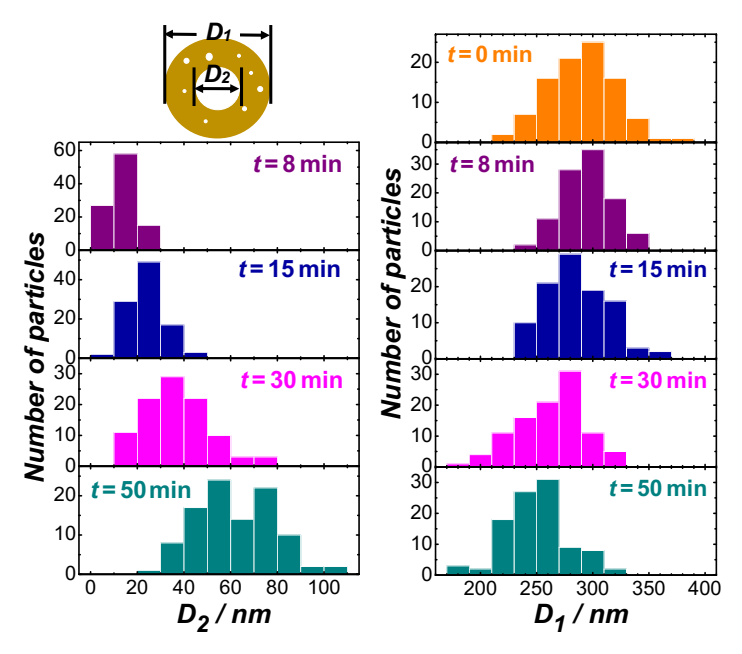


Figure S19. Distribution of D_1 and D_2 of the nanorings formed at various time spots during the covellite-to-digenite phase transitions. D_1 and D_2 were defined as outer and inner diameters of the nanorings, respectively.

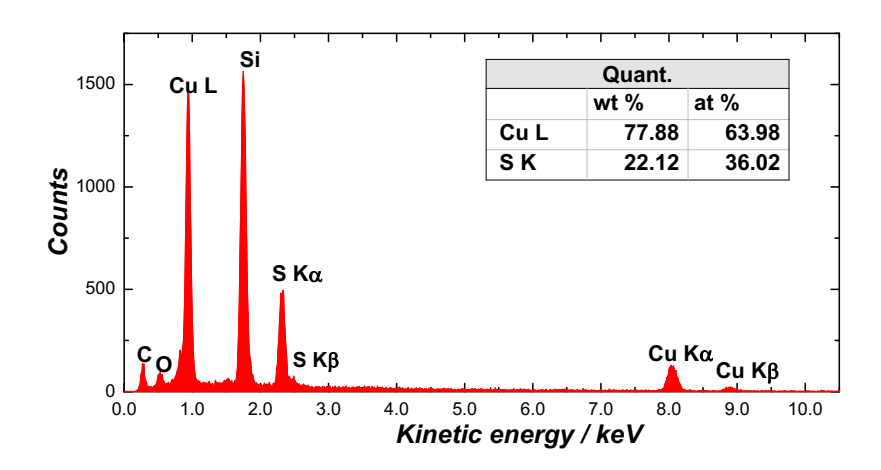


Figure S20. EDX spectrum of Cu_{1.8}S nanorings. The weight and atomic percentages of Cu and S were quantified based on the intensities of the Cu L and S K lines, respectively. The peak centered at 1.75 keV was the signals from the Si substrate.

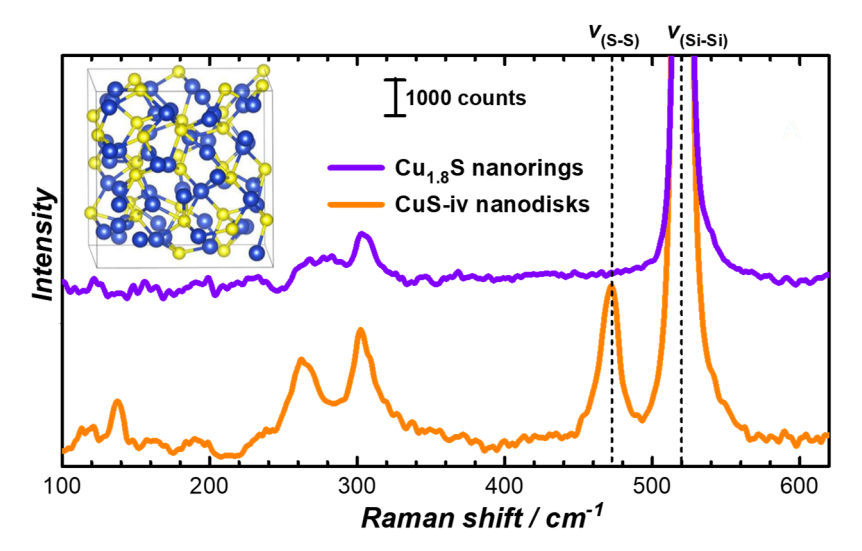


Figure S21. Raman spectra of Cu_{1.8}S nanorings and CuS-iv nanodisks. The excitation wavelength was 785 nm and the power of the excitation laser focused on the samples was 5.0 mW. The spectral integration time was 30 s. The nanodisks and nanorings were both dispersed on Si substrates. The characteristic peaks of the S-S bond and Si-Si bond stretching modes were centered at 472 and 520 cm⁻¹, respectively. A ball-and-stick model illustrating the unit cell structure of digenite (Cu_{1.8}S) was shown in the inset (Reprinted with permission from Xu, Q.; Huang, B.; Zhao, Y. F.; Yan, Y. F.; Noufi, R.; Wei, S. H. Crystal and Electronic Structures of Cu_xS Solar Cell Absorbers. *Appl. Phys. Lett.* **2012**, *100* (6), 061906. Copyright 2012 American Institute of Physics).

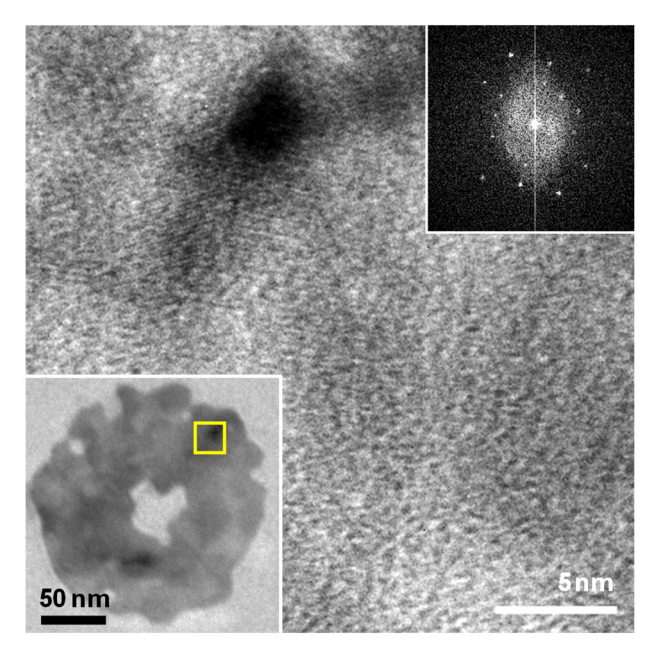


Figure S22. HRTEM image of a selected region within a Cu_{1.8}S nanoring. The TEM image of the entire nanoring and the FFT pattern of the HRTEM image were shown in the lower-left and upper-right insets, respectively.

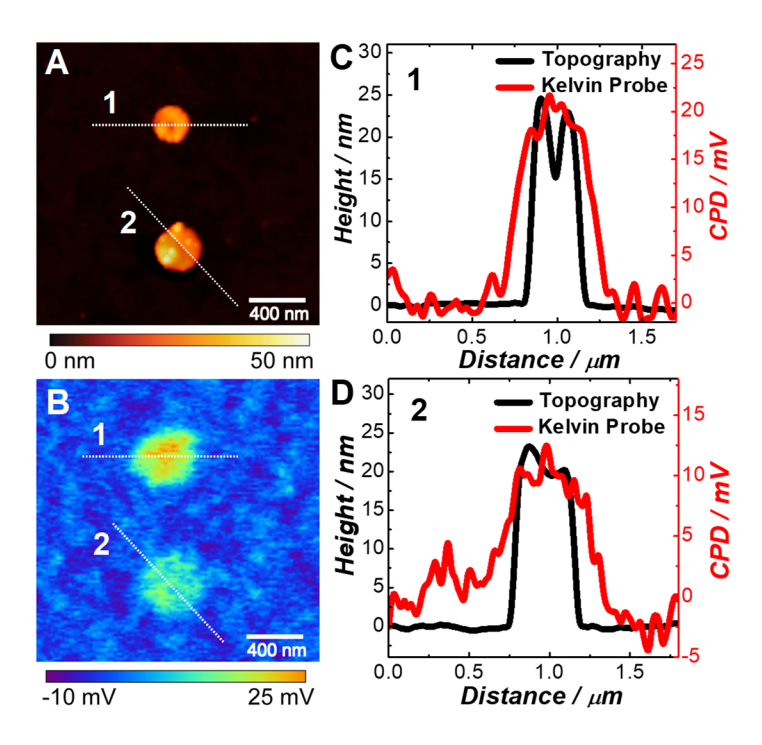


Figure S23. (A) AFM and (B) KPFM images of a Cu_{1.8}S nanoring (line 1) and a CuS-v nanodisk (line 2) on the same substrate. Topographic and CPD profiles of (C) along the line 1 across the Cu_{1.8}S nanoring and (D) along the line 2 across the CuS-v nanodisk.